Nuclear envelope rupture in cardiomyocytes orchestrates early transcriptomic changes and immune activation in *LMNA*-DCM that are reversed by LINC complex disruption

Noam Zuela-Sopilniak*[,1,2], Julien L.P. Morival*[,1,2], Ioannis Ntekas[2], Margaret A. Elpers[1,2], Rohit Agarwal[2], Sarah J. Henretta[1,2], Jacob D. Odell[1,2], Iwijn De Vlaminck[2], and Jan Lammerding[#,1,2]

[1] Weill Institute for Cell and Molecular Biology, Cornell University, Ithaca, NY, USA
[2] Meinig School of Biomedical Engineering, Cornell University, Ithaca, NY, USA
* These authors contributed equally
[#] Corresponding author; email: jan.lammerding@cornell.edu, Weill Hall, Room 235, Cornell University, Ithaca, NY 14853, USA

Abstract

Mutations in the *LMNA* gene, which encodes the nuclear envelope (NE) proteins lamins A and C, cause dilated cardiomyopathy (*LMNA*-DCM) and other diseases. The pathogenic mechanisms for *LMNA*-DCM remain poorly understood, limiting current treatment options and leading to high mortality amongst patients. We developed a mouse model with inducible, cardiomyocyte-specific *Lmna* deletion (*Lmna* cKO) and performed comprehensive bulk, single-nucleus, and spatial transcriptomic analyses across disease progression. Our analysis identified key disease-driving genes involved in cellular responses to DNA damage, cytosolic pattern recognition receptor signaling, and innate immunity that originated from two disease-specific cardiomyocyte subpopulations. Spatial mapping revealed aberrant interactions between these cardiomyocytes, fibroblasts, and immune cells, contributing to tissue-wide transcriptional changes in *Lmna* cKO hearts. Concurrent cardiomyocyte-specific disruption of the LINC complex, which transmits cytoskeletal forces to the nucleus, substantially reduced NE rupture in *Lmna* cKO cardiomyocytes, normalized expression of more than half of the dysregulated genes, and dramatically improved cardiac function and survival in *Lmna* cKO mice. These findings suggest that NE rupture in *Lmna* cKO cardiomyocytes triggers cytosolic DNA sensing pathways and maladaptive cell-cell communication with fibroblasts and immune cells, leading to fibrosis and inflammation driving *LMNA*-DCM pathogenesis.

Keywords:

Cell-cell-communication, DNA damage, laminopathy, nuclear damage, transcriptomics

Introduction

Lamins A and C (lamin A/C) are nuclear intermediate filaments that provide structural support to the nucleus and regulate numerous cellular processes, such as chromatin organization, nuclear pore positioning, signal transduction, transcriptional regulation, and DNA damage repair[1–3]. Inherited or de novo mutations in the *LMNA* gene cause a group of disorders known as laminopathies, and although lamins A and C are expressed in nearly all tissues, most *LMNA* mutations primarily affect striated muscle and tendons. *LMNA*-related dilated cardiomyopathy (*LMNA*-DCM) is the most prevalent laminopathy and has a worse clinical prognosis compared to other congenital forms of DCM[4–7], frequently resulting in sudden cardiac death, even in the absence of systolic dysfunction[5]. Currently, no effective therapies exist for *LMNA*-DCM. Furthermore, the molecular pathogenic mechanism for *LMNA*-DCM remains largely unresolved, presenting a major hurdle in developing effective treatment strategies.

A major open question in the study of striated muscle laminopathies is whether the tissue-specific phenotypes arise from disrupted lamina-chromatin interactions and altered transcription factor binding ("gene regulation hypothesis") or from impaired structural function of the nuclear lamina that results in NE rupture in mechanically stressed tissue ("structural hypothesis")[3,8]. In support of the structural hypothesis, *LMNA* mutations linked to striated muscle disease often impair lamin filament assembly, resulting in mechanically fragile nuclei and increased incidence of NE rupture[9–13]. NE rupture, although typically repaired rapidly[14–17], can lead to DNA damage and activate cytosolic DNA sensing pathways, such as cGAS/STING[9,14,15,18,19], which might trigger additional pathogenic signaling cascades that lead to cardiac dysfunction. However, it is unclear whether NE ruptures are indeed the trigger for cardiac functional decline.

Previous studies using mouse models of laminopathies and late-stage patient tissue have identified several signaling pathways to be misregulated in *LMNA*-DCM, including AMP-activated protein kinase (AMPK), myocardin-related transcription factor (MTRF), extracellular signal-regulated kinase 1/2 (ERK1/2), protein kinase C (AKT)/mammalian target of rapamycin (mTOR), Wnt/β-Catenin, transforming growth factor-β (TGF-β), and various DNA damage response pathways[20–25]. However, despite various attempts to target these altered signaling pathways in preclinical models, none of the approaches have been curative in *LMNA*-DCM mouse models, and most have shown only modest effects on survival[22,24,26–29]. These limited curative outcomes raise the question whether the identified dysregulated pathways are indeed disease-causing or arise as downstream consequences of the failing heart or other disease-associated processes.

Here, we address these questions by performing a multi-level transcriptomic analysis in left ventricle tissue obtained from an inducible *LMNA*-DCM mouse model (*Lmna* cKO), analyzing both early and late stages of disease. By examining transcriptional changes occurring early in disease, the high sensitivity of bulk-RNA sequencing allowed us to identify the activation of cGAS-independent cytosolic pattern recognition receptor (PRR) pathways, which likely respond to exposure of genomic DNA to the cytoplasm upon NE rupture[30,31], triggering innate immune activation and cardiac inflammation. Single-nucleus

RNA sequencing identified two disease-specific cardiomyocyte subpopulations that were responsible for these tissue-level transcriptomic changes in *Lmna* cKO hearts, and which are predicted to activate fibroblasts and innate immune cells through altered cellular communication. Our spatial analysis validated these findings and revealed increased spatial proximity between the disease-specific cardiomyocyte subpopulations, activated fibroblasts and immune cells in *Lmna* cKO cardiac tissue sections. Supporting a crucial role of NE rupture in driving many of the pathogenic transcriptomic changes in *Lmna* cKO hearts, concurrent cardiomyocyte-specific disruption of the Linker of Nucleoskeleton and Cytoskeleton (LINC) complex[9,10], which reduces the physical stress on diseased cardiomyocytes[32–35], significantly reduced NE ruptures and rescued the expression of approximately half of the dysregulated genes in *LMNA*-DCM hearts, including many of those involved in PRR and inflammation. Intriguingly, LINC complex disruption resulted in near complete rescue of cardiac function and extended survival of *Lmna* cKO mice from weeks to over one year. Together, our findings offer new insight into the molecular mechanisms driving *LMNA*-DCM and offer new targets to focus on for future therapeutic studies.

Results

Cardiomyocyte-specific depletion of lamin A/C in adult mice causes severe dilated cardiomyopathy

We generated mice with inducible, cardiomyocyte-specific lamin A/C depletion (*Lmna* cKO) using Cre-mediated deletion of the *Lmna* gene through a tamoxifen-responsive Cre driven by the α-myosin heavy chain promoter (αMHC-MerCreMer::*Lmna*$^{fl/fl}$). The *Lmna* cKO mice offer several key advantages for identifying disease-driving mechanisms. Unlike complete lamin A/C deletion, this model produces a reduction in lamin A/C protein levels that closely mirrors that observed in many clinical cases of *LMNA*-DCM[6,36–38]. In addition, inducing lamin A/C depletion in adulthood allowed us to disentangle the effects of lamin A/C on cardiac development from their role in cardiac function. The inducible, cardiomyocyte-specific *Lmna* deletion also reduces confounding effects present in many commonly used *LMNA*-DCM animal models, such as large variability in disease onset and severity between animals, involvement of multiple tissues, and differences in animal size and motility across genotypes[39–43]. Following tamoxifen treatment of adult *Lmna* cKO mice (Figure 1A), we observed a ≈50-70% reduction in lamin A levels in cardiomyocytes by 11 days post-injection (dpi), compared to tamoxifen-treated littermate controls that expressed the MerCreMer recombinase but lacked the floxed *Lmna* alleles (*Lmna* cWT) (Figure 1B-C). Lamin A levels in non-cardiomyocytes were not affected (Figure 1B; Suppl. Figure S1A), as expected. Immunofluorescence staining for lamin A/C showed a similar trend to lamin A, albeit with a smaller effect size, likely due to weaker antibody labeling (Suppl. Figure S1A-B). Since the anti-lamin A antibody produced better labeling in cardiac tissue sections than the anti-lamin A/C antibody, and results obtained with this antibody matched those of a recent study in the same genetic model[29], subsequent results are primarily based on immunofluorescence labeling for lamin A. Remarkably, even the partial depletion of lamin A/C in tamoxifen-treated *Lmna* cKO mice was sufficient to trigger rapid

development of severe DCM (Figure 1D). Histological analysis demonstrated increased cardiac fibrosis in *Lmna* cKO hearts already at 11-dpi, followed by substantial left ventricular enlargement of *Lmna* cKO hearts by 25-dpi (Figure 1D-E; Suppl. Figure S1E). Echocardiographic analysis revealed a reduction in cardiac function in tamoxifen-treated *Lmna* cKO mice at 11-dpi that progressively worsened by 25-dpi (Figure 1F; Suppl. Figure S1F-I). In contrast, tamoxifen-treated *Lmna* cWT controls maintained normal cardiac morphology and function (Figure 1D-F).

Consistent with the severely impaired cardiac function, tamoxifen-treated *Lmna* cKO mice had substantially reduced survival compared to *Lmna* cWT controls (Figure 1G) and vehicle-only treated controls (Suppl. Figure S1D). Male *Lmna* cKO mice died on average by 22-dpi, whereas female *Lmna* cKO mice lived until 34-dpi, despite similar depletion of lamin A as the male mice (Figure 1C; Suppl. Figure S1C and S3B). This sex-specific difference in survival is consistent with previous reports in other *LMNA*-DCM mouse models[44]. Tamoxifen-treated *Lmna* cWT controls did not exhibit premature death (Figure 1G), indicating that the Cre recombinase had no cardiotoxic effects at the administered tamoxifen dose. Intriguingly, whereas other striated laminopathy mouse models commonly show external signs of disease, such as loss of body weight and reduced motility[45], *Lmna* cKO mice died suddenly following lamin A/C depletion, without preceding weight loss (Figure 1H) or other external indications such as impaired mobility. This sudden cardiac death prior to other external indications mirrors symptoms in *LMNA*-DCM patients. Collectively, these findings indicate that even partial reduction of lamin A/C protein levels in cardiomyocytes results in severe and rapid-onset DCM[6,36–38].

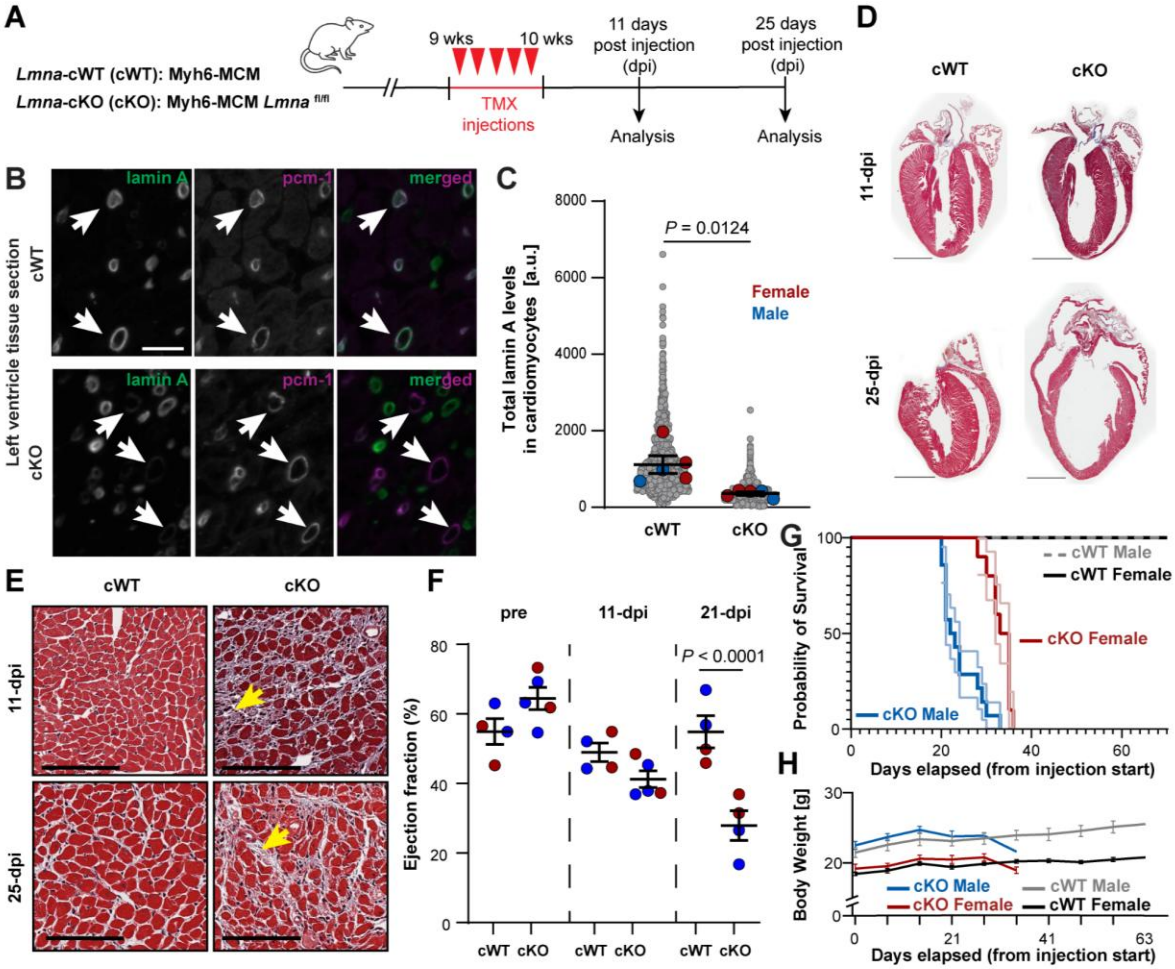

Figure 1: Cardiac-specific lamin A depletion in adult mice causes rapid onset dilated cardiomyopathy. (A) *Lmna* cWT (cWT) and *Lmna* cKO (cKO) mice were injected with 30 mg/kg tamoxifen for 5 consecutive days, starting at 9-10 weeks of age. Following a washout period, cardiac tissues were collected for analysis at two time points: 11 days post-injection (dpi), signifying a stage where DCM has not fully developed, and 21-25 dpi, in which disease is already well pronounced. Functional cardiac measurements (echocardiography) were performed at the same time points. **(B)** Representative immunofluorescence images of cardiac tissues from *Lmna* cWT (top) and *Lmna* cKO (bottom) mice labeled for lamin A (green) and Pcm-1 (magenta), a cardiomyocyte-specific nuclear marker. Scale bar 20 µm. Arrows indicate representative cardiomyocytes. **(C)** Quantification of total lamin A levels in cardiomyocytes showing a significant depletion of lamin A levels in *Lmna* cKO mice. Larger colored circles represent average values for individual male (blue) or female (red) mice. Smaller gray circles represent individual cardiomyocytes. $N = 5$ animals per genotype. Statistics are based on the mean values of individual animals. **(D)** Representative images of whole hearts stained with Masson's trichrome showing progressive thinning of the left ventricle free wall and enlargement of *Lmna* cKO hearts. Scale bar 2 mm. **(E)** Masson's trichrome staining of heart sections. Yellow arrows indicate collagen deposition in *Lmna* cKO hearts at both early (11-dpi) and late (25-dpi). Scale bar: 100 µm. **(F)** Left ventricular ejection fraction (EF), given as a percentage, measured by echocardiography. Symbols represent %EF of individual mice. Red symbols denote female mice, blue male mice. Error bars represent mean ± s.e.m. **(G)** Kaplan-Meier survival plot for *Lmna* cWT mice ($N = 14$ males and 11 females) and *Lmna* cKO mice ($N = 14$ males and 10 females). **(H)** Body weight measurements performed during the survival study on the mice in panel (G) before (day 0) and after tamoxifen (TMX) injections.

Transcriptomic profiling reveals early and progressive gene dysregulation in *LMNA*-DCM hearts.

To comprehensively characterize the transcriptional changes resulting from cardiac-specific *Lmna* deletion in mouse hearts during disease progression, we performed bulk (RNA-seq), single-nucleus (snRNA-seq), and spatially resolved RNA sequencing (Curio Biosciences, Seeker) on left ventricular free wall tissue from tamoxifen-treated *Lmna* cKO mice and *Lmna* cWT controls at 11- and 25-dpi (Figure 2A), corresponding to early disease onset and severe cardiac dysfunction, respectively (Figure 1D-F). We initially focused on bulk RNA-seq data to capture broad transcriptional shifts in *LMNA*-DCM cardiac tissue and to identify key genes and pathways for deeper investigation at the cellular and spatial level. We found that transcriptional differences between *Lmna* cKO and *Lmna* cWT hearts were already detectable at 11-dpi and became more pronounced by 25-dpi (Figure 2B). The number of differentially expressed genes (DEGs) increased from 86 at 11-dpi to 2,951 at 25-dpi (Suppl. Figure S2A). The majority of DEGs showed increased expression in the *Lmna* cKO samples (Suppl. Figure S2B), suggesting that *Lmna* cKO hearts have a progressive activation of transcriptional programs. Despite the sex-specific differences in survival (Figure 1G), we did not detect any transcriptional differences between male and female *Lmna* cKO mice (Suppl. Figure S3A). Consequently, we combined data from male and female mice in subsequent analyses to increase their statistical power.

Given the only subtle transcriptional differences present at 11-dpi (Figure 2B), we hypothesized that some early changes in gene expression that are statistically significant may fall below our stringent threshold criteria for DEGs, (i.e., $|\log_2 \text{fold change}| \geq 1$), yet might still contribute to disease pathogenesis. To identify which dysregulated genes are likely to drive disease progression, we developed an analysis pipeline that uncovered 496 genes that were already statistically significant at 11-dpi and whose change in expression increased further over time, reaching the $|\log_2|$-fold threshold for DEG by 25-dpi (Suppl. Figure S2A). We termed these genes ‘emerging DEGs’ (eDEGs) and hypothesized that these eDEGs play crucial roles in *LMNA*-DCM pathogenesis. Indeed, hierarchical clustering of samples based on eDEG expression created distinct separation based on genotype and timepoint (Figure 2C), demonstrating that our methodology enables the enhanced detection of genes already dysregulated early in disease and thus likely constituting disease drivers. In contrast to the 496 eDEGs, we identified only 12 genes that were statistically significant at 11-dpi but that reversed the direction of change (e.g., from up- to down-regulated) at 25-dpi (Suppl. Figure S2C, D), supporting the interpretation that the eDEGs represent early pathogenic changes that become more pronounced over time.

To uncover disease-driving biological processes mediated by the identified eDEGs, we performed comparative Gene Ontology (GO) analysis contrasting eDEGs with DEGs identified at 25-dpi (Figure 2D)[46,47]. Among the top 10 overrepresented GO cluster terms in both gene sets were several processes previously linked to lamin A/C deficiency, such as increased MAPK activation[48] and apoptosis[49]. In addition, eDEGs were enriched for terms associated with inflammation, innate immunity, and cardiac function.

222 **Two cardiomyocyte subpopulations predominantly account for early disease-**
223 **driving changes in gene expression in lamin A/C depleted hearts**
224
225 To distinguish the individual transcriptional contribution of different cell types to the overall
226 response, we next focused on the snRNA-seq dataset. Cell type annotation identified
227 many of the expected cell types previously found in left ventricular tissue[50], including
228 cardiomyocytes, immune cells, fibroblasts, and endothelial cells (Figure 2E).
229 Cardiomyocyte nuclei clustered into five individual subpopulations, two of which, CM3
230 and CM5, progressively expanded over time (Figure 2F) and were represented only in
231 *Lmna* cKO hearts (Figure 2G), mirroring the increased transcriptional divergence we
232 observed between *Lmna* cKO and *Lmna* cWT control hearts (Figure 2B). Spatial
233 transcriptomics applying Curio Seeker (slide-seq[51]) analysis to cryo-sectioned left
234 ventricles enabled us to map the identified cardiomyocyte subpopulations based on their
235 snRNA-seq transcriptional profiles and to further validate that the CM3 and CM5
236 cardiomyocyte subpopulations are present in the *Lmna* cKO hearts at both 11- and 25-
237 dpi, but not in the *Lmna* cWT hearts (Figure 2H, Suppl. Figure S4).
238
239 To assess the contribution of disease-specific cell populations to pathogenic gene
240 expression, we compared the transcriptomic profile of individual cell subpopulations
241 identified in the snRNA-seq analysis to the eDEGs identified in the bulk RNA-seq data.
242 Remarkably, the cardiomyocyte subpopulations CM3 and CM5 together accounted for
243 over 40% of all eDEGs (Figure 2I, Suppl. Figure S5A-B), despite comprising only 11% of
244 total cardiomyocyte nuclei (Figure 2F). The eDEGs detected in the CM3 and CM5
245 subpopulations enriched for similar GO terms to all eDEGs, namely, immunity, apoptosis,
246 and cardiac function (Suppl. Figure S5C). Together, these findings suggest that the
247 identified disease-specific cardiomyocyte CM3 and CM5 subpopulations are involved in
248 promoting *LMNA*-DCM pathogenesis.
249

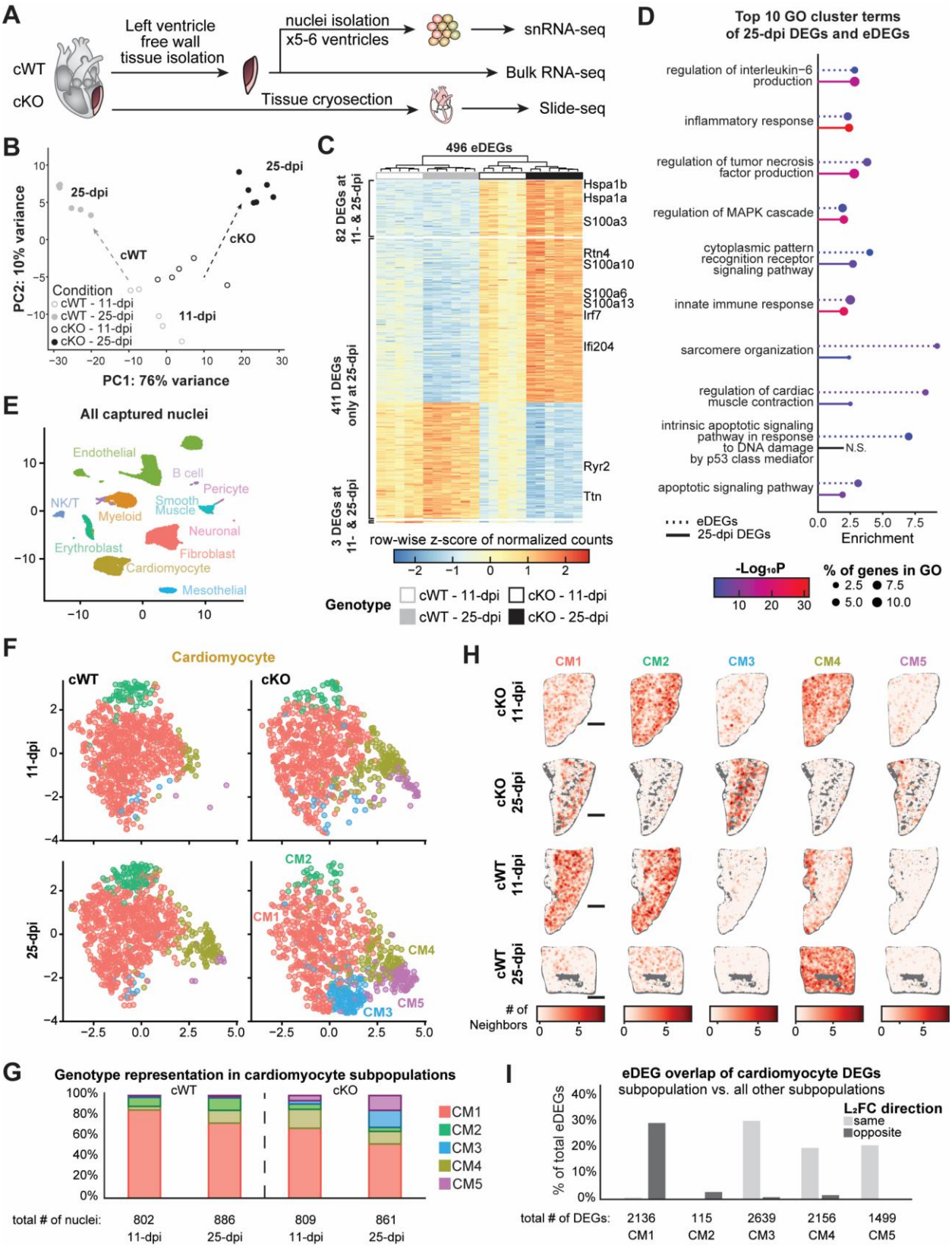

Figure 2: *LMNA*-DCM-associated eDEGs are mainly associated with two disease-specific cardiomyocyte subpopulations. (A) Schematic depiction of the experimental setup for transcriptomic

studies on *Lmna* cKO (cKO) and *Lmna* cWT (cWT) hearts. Bulk RNA, single-nucleus (snRNA-seq), and spatial transcriptomic (Curio Seeker) assays were performed on isolated left ventricular free wall tissue or cryosectioned hearts. **(B)** Principal components analysis (PCA) plot of bulk RNA-seq sample from all experimental conditions. Dashed lines and arrows indicate progressive separation of samples from different genotypes (*Lmna* cKO and *Lmna* cWT) from 11- to 25-days post injection (dpi). **(C)** Heatmap of row-wise z-score normalized read counts for eDEGs. Rows are separated based on meeting DEG requirements at both timepoints (85 genes, top and bottom sections) or meeting DEG requirements at 25-dpi and significant difference by 11- dpi (411 genes, middle section). Columns, indicating individual samples, were sorted using unbiased hierarchical clustering, with experimental conditions denoted below by color. Select genes identified throughout the study are highlighted. **(D)** Lollipop plot of top Gene Ontology (GO) cluster terms enrichment among emerging differentially expressed genes (eDEGs, dashed line) and 25-dpi DEGs (continuous line). Not-significant (N.S.) terms are denoted. **(E)** UMAP plots of captured snRNA-seq nuclei integrated in cWT (left) and cKO (right) samples. Individual colors represent unique cell type clusters. Color shades indicated early (11-dpi, light) and late (25-dpi, dark) timepoints. **(F)** UMAP plots of cardiomyocyte subpopulations from integrated snRNA-seq data, across genotype (left and right) and timepoint (top and bottom). Individual colors represent unique cardiomyocyte-specific subpopulations identified (CM1-5). **(G)** Bar chart of the composition of individual cardiomyocyte subpopulations in each experimental condition as the percentage of total sequenced cardiomyocyte nuclei. Total number of sequenced nuclei are indicated for each subgroup. **(H)** Spatial neighborhood enrichment maps for cardiomyocyte populations (CM1–CM5) across *Lmna* cKO and *Lmna* cWT heart left ventricles at 11- and 25-dpi. At each spot, the red intensity reflects the number of its 10 nearest spatial neighbors assigned to the corresponding CM type, indicating local spatial clustering. Scale bars = 500 µm. **(I)** Bar chart of the percentage of total emerging DEGs (eDEGs, identified in bulk RNA-seq) that overlap with subpopulation-specific DEGs. Bar plot color indicates whether the eDEG and corresponding DEG are in the same (both up- or down-regulated; light gray) or opposite (one up- and one down-regulated; dark gray) fold change direction. The total number of DEGs is indicated below each condition.

Lamin A/C-depleted hearts exhibit transcriptomic evidence of cytosolic DNA sensing pathway activation

Several groups have previously reported the presence of NE damage in patient samples and early-stage mouse models of striated laminopathies, which often display chromatin protrusions and NE ruptures[9,25,29,39,52,53]. The NE ruptures can be readily visualized by transient accumulation of the barrier-to-autointegration factor (BAF) protein at the NE (Figure 3A)[14], where BAF contributes to NE repair[16,17]. Consistent with the increased presence of NE rupture in striated muscle laminopathies and the resulting cytoplasmic DNA leakage, the eDEGs were significantly enriched for the GO term “cytoplasmic pattern recognition receptor signaling pathway”. This GO term encompasses molecules involved in cytosolic DNA sensing pathways, including cyclic GMP-AMP synthase (cGAS), one of the major cytoplasmic DNA sensors, and its target STING, which acts as a central node for downstream activation of NF-κB and interferon-regulatory factors (IRFs) in the inflammatory response pathway[30,54]. Ingenuity Pathway Analysis (IPA) revealed that many of the top 25 predicted upstream regulators of the eDEGs are components of the cytosolic DNA-sensing pathway, including Sting1, Irf3, Irf7, Myd88, and NF-κB (*NFKB*) (Table 1). Although a GO term analysis of eDEGs associated with subpopulations CM3 and CM5 did not find the same cytosolic DNA sensing pathway enrichment (Suppl. Figure S5C), IPA did identify several upstream regulators involved in the cytosolic DNA-sensing signaling cascade, including Toll-like receptor-9 (TLR9), p53 (TP53), Interleukin-6 (IL6), NF-κB (NFkB), Interleukin-1 (IL1A/B), MyD88, and interferon-γ (IFNG) (Figure 3B). Furthermore, both the single-nucleus and spatial data revealed within the CM3 and CM5 subpopulations a particular enrichment of the GO terms “inflammatory response” and

304 “regulation of defense” (Figure 3 C-E, Suppl. Figure S6A-B), which include cytosolic DNA-
305 sensing molecules.
306
307 Notably, despite the significant activation of cytosolic DNA-sensing pathways, very few
308 cardiomyocytes expressed *cGAS* or *Sting*, and neither was significantly expressed in the
309 CM3 and CM5 subpopulations, based on the snRNA-seq data (Suppl. Figure S7A-D).
310 This observation is in agreement with recent studies reporting that cGAS is essentially
311 absent in cardiomyocytes, and that deletion of either *cGas* or *Sting* does not rescue
312 cardiomyopathy in *LMNA*-DCM mouse models[29,50,55]. The absence of *cGAS*/*Sting*
313 activation prompted us to look for alternative cytosolic DNA sensors expressed in
314 cardiomyocytes that could contribute to the observed inflammatory response. Based on
315 the snRNA-seq (Figure 3F) and spatial transcriptomic datasets (Figure 3G, Suppl. Figure
316 S6C), *Rtn4* stood out as a highly upregulated eDEG expressed in the CM3 and CM5
317 subpopulations. Rtn4 is a resident endoplasmic reticulum (ER) transmembrane protein
318 involved in the trafficking of toll-like receptor (TLRs), particularly TLR9, from the ER to
319 endolysosomes, where cytosolic nucleic acid-sensing TLRs can initiate a signaling
320 cascade for downstream innate immune response, independent of the cGAS/STING
321 pathway[30,31,56]. We confirmed significantly higher levels of Rtn4 protein in *Lmna* cKO
322 compared to *Lmna* cWT samples at 25-dpi using both immunofluorescence (IF) and
323 western blot analysis (Figure 3H-I, Suppl. Figure S8A). We also noticed the upregulation
324 of several genes downstream of TLR activation in the CM3 and CM5 subpopulations
325 (Suppl. Figure S9). Finally, despite the lack of *Sting* expression in *Lmna* cKO
326 cardiomyocytes, analysis of the snRNA-seq data revealed that several cardiomyocytes,
327 particularly in the CM3 subpopulations, expressed interferon gamma inducible protein 16
328 (IFI16, also known as IFI204) (Supp Figure S7E), a cytoplasmic DNA sensor that is a
329 known STING activator, but can also work independently of STING to induce the
330 formation of inflammasome complexes and the release of cytokines[57]. These findings
331 suggest that the disease-specific subpopulations CM3/CM5 might represent
332 cardiomyocytes in which exposure of genomic DNA to the cytoplasm upon NE rupture
333 triggers the activation of cytosolic DNA-sensing pathways, which leads to the production
334 of cytokines, interferons, and other inflammatory signaling pathways.
335

Top 25 predicted upstream regulators of eDEGs at 11-dpi

Upstream Regulator	Molecule Type	Predicted State	Activation z-score	-Log10(*P*-value) of Overlap	Top 10 Differentially Expressed Target Molecules in Dataset
Ifng	cytokine	Activated	6.466	30.74	Nmrk2, Cd24a, H2ac6, Hmox1, Hspa1a, Lgals3, Ccl7, Mlana, Mafa, Dbp
Tnf	cytokine	Activated	6.071	15.95	Hmox1, Hspa1a, Lgals3, Serpina3n, Serpinb1a, Ccl7, Mlana, Mafa, Klf5
Il1b	cytokine	Activated	5.073	16.02	Cd24a, H2bc8, Hmox1, Hspa1a, Serpina3n, Ccl7, Mafa, Cdkn1a, S100a3, Dbp
INTERFERON ALPHA (family)	group	Activated	4.968	12.02	Hmox1, Hspa1a, Lgals3, Serpinb1a, Cdkn1a, Tnfsf18, Cxcl2, Il1rn, Atf3, Oas1g
Il1a	cytokine	Activated	4.662	8.92	Hmox1, Serpina3n, Cdkn1a, Cxcl2, Ccl2, Il1rn, S100a10, Atf3, Sprr1a, Ccl4
Myd88	other	Activated	4.634	8.41	Hmox1, Gdf15, Tnfrsf12a, Cxcl2, Ccl2, Cebpd, Il1rn, Nppb, Maff, Ccl17
Tlr4	transmembrane receptor	Activated	4.632	11.59	Hmox1, Ccl7, Nr4a2, Cxcl2, Ddit3, Ccl2, Cebpd, Nppb, Atf3, Ccl4
App	other	Activated	4.375	10.26	Hmox1, Hspa1a, Crabp2, Lgals3, Ccl7, Cdkn1a, Gdf15, Nr4a2, Shisa3, Cxcl2
Sting1	ion channel	Activated	4.329	14.47	Cxcl2, Ddit3, Ifi27l2a, Oas1g, Oas3, Oas2, Fcgr4, Ccl4, Pnp, Irf7
NFKB (complex)	complex	Activated	4.292	14.27	Slc2a5, Cd24a, Hmox1, Serpina3n, Ccl7, Cdkn1a, Gdf15, Cgref1, Cxcl2, Dbp
Il6	cytokine	Activated	4.274	7.71	Hmox1, Serpina3n, Cdkn1a, Tnfrsf23, Hpx, Tnfrsf12a, Cxcl2, Ccl2, Cebpd, Il1rn
Irf7	transcription regulator	Activated	4.262	9.11	Ccl2, Oas1g, Oas3, Oas2, Ly6a, Ube2l6, Irf7, Ifitm3, Mx2, Phf11b
Irf3	transcription regulator	Activated	4.235	13.75	Cdkn1a, Ccl2, Ifi27l2a, Oas1g, Oas3, Oas2, Ccl4, Pnp, Ube2l6, Irf7
TP53	transcription regulator	Activated	4.212	15.38	Peg10, Hmox1, Hspa1a, Lgals3, Serpina3n, Psat1, Klf5, Cdkn1a, Ddit4l, Dbp
Csf2	cytokine	Activated	4.189	8.94	Hmox1, Cdkn1a, Ccl25, Gdf15, Nr4a2, Ifrd1, Cxcl2, Ddit3, Ccl2, Il1rn
Agt	growth factor	Activated	4.102	19.62	Hspa1b, Gabrb3, Hmox1, Nptx2, Hspa1a, Crabp2, Lgals3, Serpina3n, Ccl7, Klf5
Tgfb1	growth factor	Activated	4.095	20.08	Hmox1, Hspa1a, Lgals3, Serpina3n, Psat1, Serpinb1a, Ccl7, Cdkn1a, Gsta2, Dbp
LDL (complex)	complex	Activated	4.088	16.87	Hmox1, Ccl7, Cdkn1a, Star, Nr4a2, Cxcl2, Ccl9, Ddit3, Ccl2, Il1rn
ERK1/2 (family)	group	Activated	4.056	8.21	Cdkn1a, Star, Gnrh1, Cxcl2, Ddit3, Ccl2, Ccn2, Ccl4, S100a6, Rhoc
Irgm1	enzyme	Inhibited	-4.042	11.58	Ccl2, Ifi27l2a, Oas1g, Oas3, Oas2, Apol9a, Irf7, Ifitm3, Mx2, Ifi204
Apoe	transporter	Inhibited	-4.048	11.14	Hspa1b, Hmox1, Hspa1a, Serpina3n, Cxcl2, Ddit3, Ccl2, Il1rn, Ccn2, Atf3
Irf2bp2	transcription regulator	Inhibited	-4.094	9.55	Hmox1, Hcn1, Serpina3n, Ccl9, Scimp, Fcgr4, Cd14, Mybl1, Mmp3, Pilra
Ttc39aos1	other	Inhibited	-4.319	17.16	Ccl7, Ccl2, Oas3, Oas2, Ccl4, Ly6a, Apol9a, Ube2l6, Irf7, Ifitm3
Trex1	enzyme	Inhibited	-4.349	16.36	Cdkn1a, Ifi27l2a, Panx1, Oas1g, Oas3, Oas2, Ly6a, S100a6, Ube2l6, Gpx1
Cited2	transcription regulator	Inhibited	-4.61	9.78	Ifrd1, Cxcl2, Ccl2, Il1rn, Pou3f1, Oas1g, Oas3, Scimp, Gadd45b, Fcgr4

Table 1: Cytosolic DNA sensing signaling proteins were predicted as upstream regulators of eDEGs. Top 25 upstream regulators, identified by Ingenuity Pathway Analysis (IPA), predicted to be activated or inhibited based on 11-dpi eDEG expression differences between *Lmna* cKO and *Lmna* cWT samples. Top 10 most differentially expressed eDEGs targeted by predicted upstream regulators are displayed.

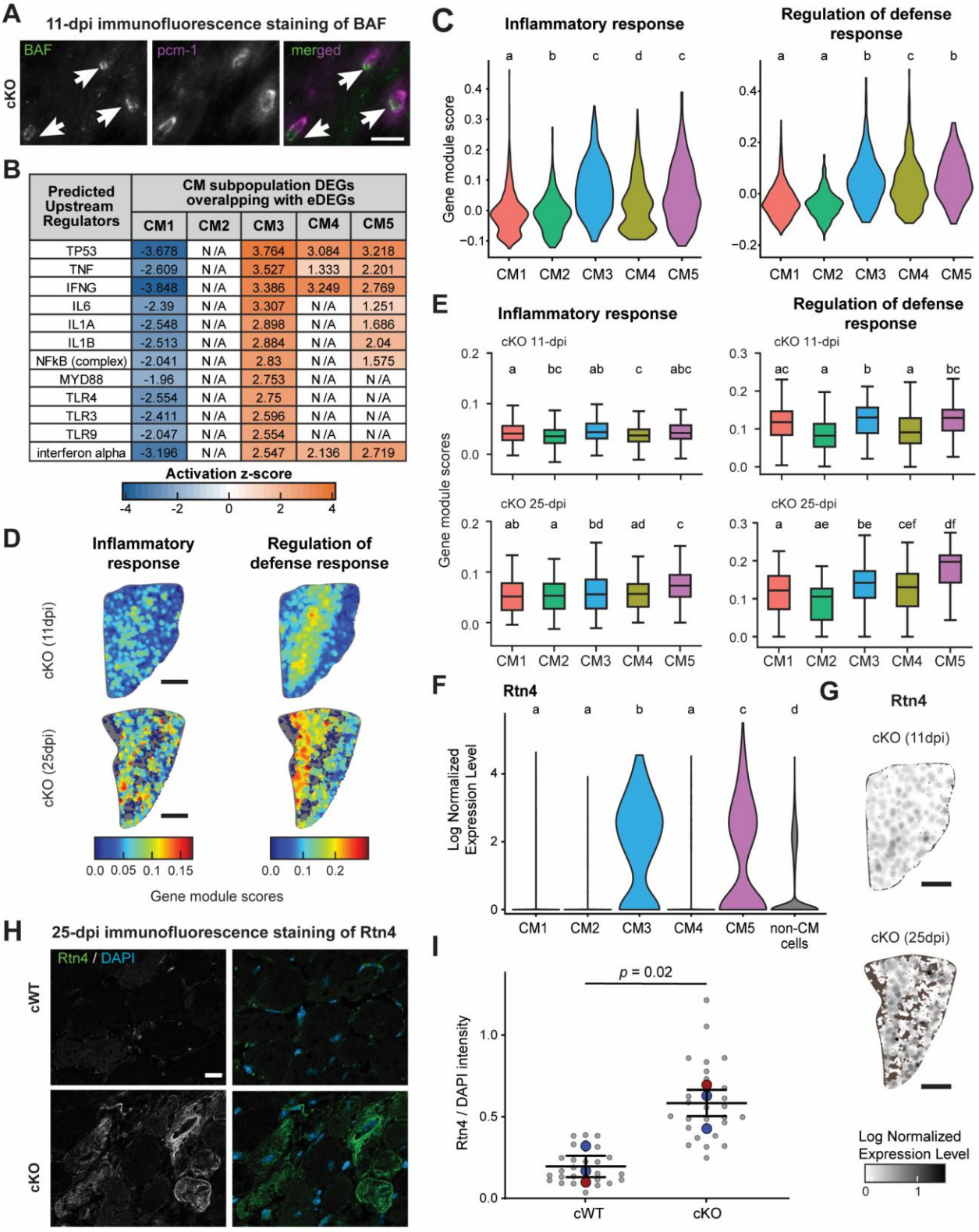

Predicted Upstream Regulators	CM subpopulation DEGs overalpping with eDEGs				
	CM1	CM2	CM3	CM4	CM5
TP53	-3.678	N/A	3.764	3.084	3.218
TNF	-2.609	N/A	3.527	1.333	2.201
IFNG	-3.848	N/A	3.386	3.249	2.769
IL6	-2.39	N/A	3.307	N/A	1.251
IL1A	-2.548	N/A	2.898	N/A	1.686
IL1B	-2.513	N/A	2.884	N/A	2.04
NFkB (complex)	-2.041	N/A	2.83	N/A	1.575
MYD88	-1.96	N/A	2.753	N/A	N/A
TLR4	-2.554	N/A	2.75	N/A	N/A
TLR3	-2.411	N/A	2.596	N/A	N/A
TLR9	-2.047	N/A	2.554	N/A	N/A
interferon alpha	-3.196	N/A	2.547	2.136	2.719

Figure 3: *Lmna* cKO hearts exhibit transcriptomic evidence of cytosolic DNA-sensing pathway activation (A) Representative immunofluorescence images of cardiac tissues from *Lmna* cKO mice at 11-dpi labeled for BAF (green) to indicate NE rupture, and Pcm-1 (magenta), a cardiomyocyte-specific nuclear marker. Scale bar 20 μm. Arrows indicate representative cardiomyocytes. **(B)** Table showing the predicted

activation of the top 40 upstream regulators involved in DNA damage and cytosolic DNA sensing pathways identified using Ingenuity Pathway Analysis (IPA) based on cardiomyocyte subpopulation (CM1-5)-specific DEGs that overlap eDEGs. N/A indicates the upstream regulator was not predicted. **(C)** Violin plots of gene module scores for GO terms "inflammatory response" (left) and "regulation of defense" (right) for individual cardiomyocyte subpopulations (CM1-5) in the integrated snRNA-seq ventricle dataset. Sets of points with the same letter above them are not significantly different, whereas different letters indicate $p < 0.05$, pair-wise Wilcoxon rank sum test with Benjamini-Hochberg *p*-value adjustment. **(D)** Spatial visualization and **(E)** boxplot of GO term gene module scores "Inflammatory response" (left) and "Regulation of defense" (right) across **(D)** the left ventricle and **(E)** individual cardiomyocyte subpopulations (CM1-5) of 11- and 25-days post-injection (dpi) *Lmna* cKO (cKO) heart tissue slices based on spatial transcriptomics. **(D)** Color scales indicate module scores. Scale bars = 500 µm. **(E)** Sets of points with the same letter above them are not significantly different. In contrast, different letters indicate $p < 0.05$, Kruskal–Wallis tests followed by pairwise Mann–Whitney U tests with Benjamini-Hochberg *p*-value adjustment. **(F)** Violin plot of normalized *Rtn4* expression across CM1-5 and all non-cardiomyocyte cells in the integrated snRNA-seq ventricle dataset. Sets of points with the same letter above them are not significantly different. In contrast, different letters indicate $p < 0.05$, Kruskal–Wallis tests followed by pairwise Mann–Whitney U tests with Benjamini-Hochberg *p*-value adjustment. **(G)** Heatmap of $\log_2$-normalized *Rtn4* expression across left ventricle of 11-dpi (left) and 25-dpi (right) *Lmna* cKO heart tissue slices based on spatial transcriptomics. **(H)** Immunofluorescence labeling for Rtn4 (gray on the left, green on the right) and nuclei using DAPI (blue) for *Lmna* cWT (top) and *Lmna* cKO (bottom) ventricles at 25-dpi. Scale bar 20 µm **(I)** Quantification of Rtn4 over DAPI intensity from representative images of *Lmna* cWT (left) and *Lmna* cKO (right) ventricles at 25-dpi. Larger colored circles represent average values for individual male (blue) or female (red) mice. $N = 3$ animals per genotype. Statistical analysis represented by *t*-test.

Lamin A/C-depleted hearts show progressive innate immune cell activation

Cytosolic DNA-sensing pathways can activate transcription factors such as NF-κB and IRF, leading to their nuclear translocation and subsequent upregulation of pro-inflammatory cytokines and type I interferons, including INF-α[30] and INF-γ[58,59]. In parallel, studies utilizing human patient samples and murine pre-clinical *LMNA*-DCM models[29,50] reported that cardiomyocytes, in response to injury, release cytokines and damage-associated molecular patterns (DAMPs), which recruit immune cells and promote inflammation and cardiac remodeling[60,61]. Consistent with these previous findings, our analysis of GO cluster terms among the eDEGs and 25-dpi DEGs revealed an enrichment for immune response and inflammation (Figure 2D), particularly associated with innate immunity. Notably, the disease-specific cardiomyocyte subpopulations CM3 and CM5 exhibited elevated expression of cytokines (*Il34*, *Il4*, *Cxcl9*, *Ccl5*) and several DAMPs, including heat shock proteins, S100 proteins, and HMGB-1 (Suppl. Figure S10). Several of these DAMPs also appeared as eDEGs, suggesting their potential involvement in promoting disease.

Our snRNA-seq analysis further revealed an increase in immune cell populations within the *Lmna* cKO hearts at 25-dpi (1376 captured nuclei), compared to the minimal cell counts (358 captured nuclei) seen in *Lmna* cWT controls (Figure 4A). Western blot analysis (Suppl. Figure S8C) and immunofluorescence labeling confirmed an increased prevalence of macrophages and monocytes in *Lmna* cKO left ventricular samples, with elevated intensity and area of the common macrophage/monocyte marker CD68 starting at 11-dpi and increasing further at 25-dpi (Figure 4B-C). Notably, unlike the emergence of disease specific cardiomyocyte subpopulations in the *Lmna* cKO hearts, none of the immune subtypes showed emergence of new, disease-specific subpopulations, but rather

398 displayed an expansion of several existing immune subpopulations in *Lmna* cKO hearts
399 during disease progression, with subpopulation ratios shifting towards Mye1 (22% to
400 32%), Mye2 (24% to 28%), Mye4 (13% to 23%), and NKT2 (29% to 51%) (Figure 4A,
401 Suppl. Figure S11A). Using established gene expression markers[62], we identified Mye2
402 & Mye4 as tissue resident macrophages and Mye1 as infiltrating macrophages (Figure
403 4D). These data show that infiltrating macrophages (Mye1) increasingly contribute to the
404 myeloid cell population in *Lmna* cKO hearts over time. However, the concurrent
405 proliferation of resident macrophages (Mye2 and Mye4) indicates that both recruitment
406 and expansion of tissue-resident immune cells drive the evolving immune landscape,
407 potentially amplifying inflammatory signaling and disease progression. Immuno-
408 fluorescence co-staining for the monocyte/macrophage marker CD68 and Rtn4 revealed
409 increased spatial proximity between cells expressing Rtn4 and CD68-positive cells in the
410 *Lmna* cKO hearts compared to cWT controls (Figure 4E-F). This spatial proximity
411 supports a model in which Rtn4-mediated release of cytokines from cardiomyocytes with
412 NE rupture leads to the local recruitment and expansion of innate immune cells to drive
413 the inflammation and remodeling observed in *LMNA*-DCM.
414

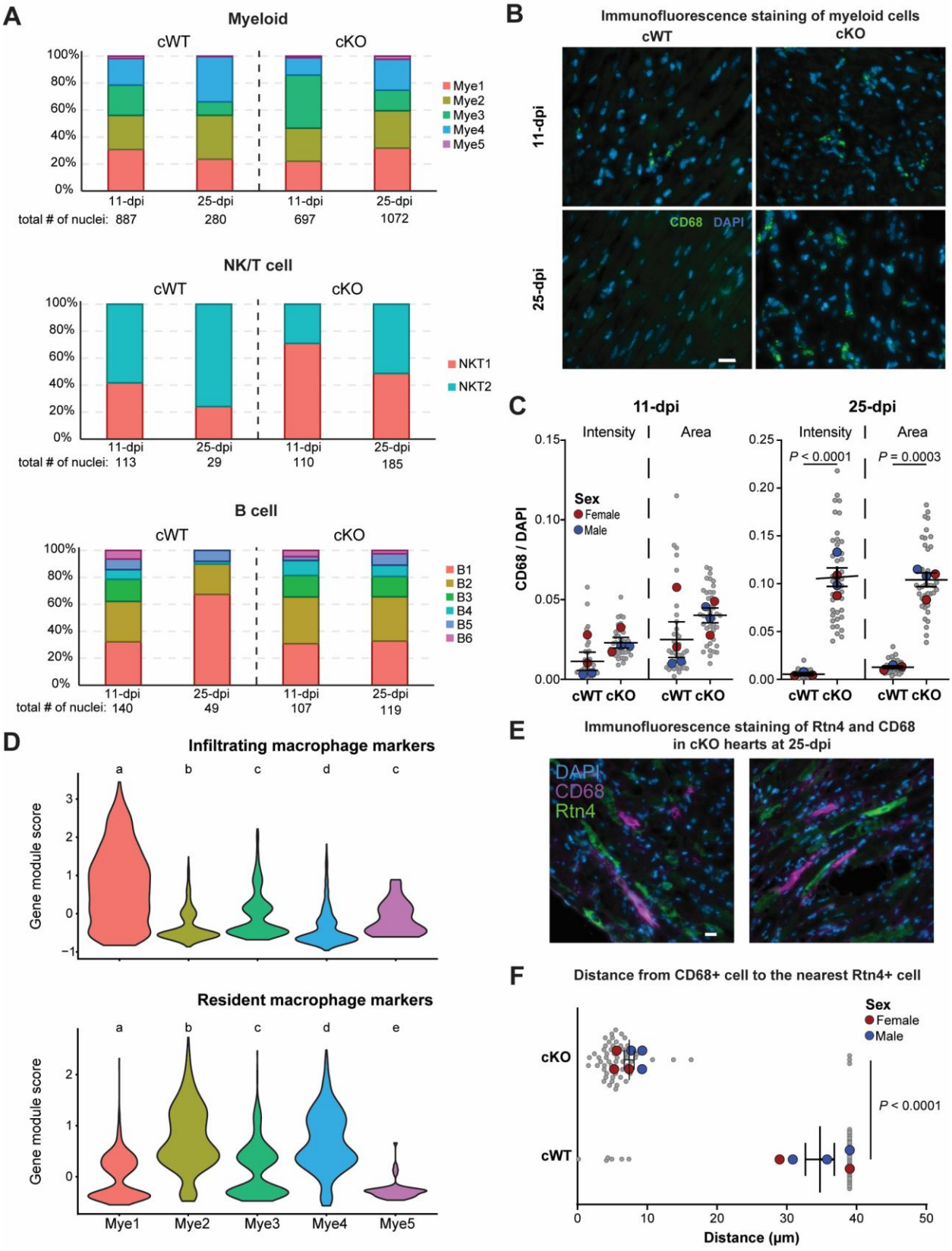

Figure 4: Cytoplasmic DNA sensing initiates immune infiltration in *LMNA*-DCM hearts. (A) Bar chart of the number of nuclei captured in each genotype within individual immune cell subclusters and in total.

(B) Representative images of cardiac tissue sections from *Lmna* cWT (left, cWT) and *Lmna* cKO (right, cKO) hearts at 11-dpi (top) and 25-dpi (bottom), labeled with antibodies against the myeloid cell surface marker CD68 (green) and the DNA stain DAPI (blue). Scale bar 20 μm. **(C)** Quantification of CD68 fluorescence intensity normalized to DAPI intensity (left side of graph) and cardiac tissue section area positive for CD68 (right side of graph) normalized to area positive for DAPI for *Lmna* cKO and cWT cardiac tissue sections, collected at 11-dpi (left) and 25-dpi (right). Larger colored circles represent average values for individual male (blue) or female (red) mice. Smaller gray circles represent individual fields of view. N = 4 animals per genotype. Statistical analysis by Tukey Honest Significant Difference of one-way ANOVA test. **(D)** Violin plot of gene module scores for gene markers associated with infiltrating (left) and resident (right) macrophages across individual myeloid cardiomyocyte subpopulations (Mye1-5) in the integrated snRNA-seq ventricular dataset. Sets of points with the same letter above them are not significantly different, whereas different letters indicate $p < 0.05$, pair-wise Wilcoxon rank sum test with Benjamini-Hochberg p-value adjustment. **(E)** Representative images of cardiac tissue sections from *Lmna* cKO hearts at 25-dpi stained with antibodies against the myeloid cell surface marker CD68 (magenta), the cytoplasmic DNA sensing component Rtn4 (green), and with a DAPI nuclear dye (blue). Scale bar: 20 μm **(F)** Nearest neighbor analysis of *Lmna* cKO (top) and *Lmna* cWT (bottom) hearts representing the distance in μm of Rtn4 positive cells from CD68 positive cells. Larger colored circles represent average values for individual male (blue) or female (red) mice. Smaller gray circles represent individual fields of view. N = 5-6 animals per genotype. For statistical comparison, we selected 40 μm as an arbitrary threshold for lack of spatial proximity. Statistical analysis by Tukey Honest Significant Difference of one-way ANOVA test.

Lamin A/C depleted cardiomyocytes affect non-cardiomyocyte gene expression through altered cell-cell communication

Inflammatory cytokines and DAMPs can lead to activation of immune cells[63] and myofibroblasts[64,65] through signaling pathways that, in turn, induce further transcriptomic changes. We reasoned that non-cardiomyocyte cells would thus display disease-specific transcriptomic signatures in response to cell-cell signaling initiated by pathogenic cardiomyocytes. Our snRNA-seq analysis identified several subpopulations in *Lmna* cKO non-cardiomyocyte cells with distinct gene expression changes (Suppl. Figures S11A-C), despite not being depleted for lamin A/C. In agreement with the general transcriptomic trend (Figure 2B), fibroblasts had substantially higher amounts of aberrant gene expression between *Lmna* cKO and *Lmna* cWT hearts at the 25-dpi timepoint (608 DEGs at 11-dpi, 4818 DEGs at 25-dpi; Figure 5A). In contrast, over 65% of 25-dpi DEGs in immune cells were already differentially regulated at 11-dpi (Figure 5A). These findings suggest that the contribution of fibroblasts to pathogenic gene expression takes place at the more advanced disease stage, whereas immune cells gene misregulation is initiated early in disease.

Transcriptomic changes in non-cardiomyocyte *Lmna* cKO cells could either be the result of communication from the *Lmna*-depleted cardiomyocyte or in response to global changes in the failing heart. To distinguish these mechanisms, we applied the CellChat[66] algorithm to our snRNA-seq transcriptomic data to compare cell-cell communication between *Lmna* cKO and *Lmna* cWT hearts at each timepoint. Cell-cell communication was overall downregulated in *Lmna* cKO versus *Lmna* cWT hearts at 11-dpi but increased by 25-dpi (Figure 5B). Fibroblasts had a particularly strong shift from down- to up-regulated interaction strength between the 11- and 25-dpi timepoints, mirroring the increase in the number of DEGs over time (Figure 5A) and driving most of the outgoing signaling to innate immune cells (myeloid and NK/T cells) during the 25-dpi timepoint.

467 Myeloid and NK/T cell interactions were also upregulated at 25-dpi, further corroborating
468 the involvement of innate immunity as opposed to adaptive immunity in disease
469 progression. Consistent with this idea, B cells had decreased incoming communication
470 from all other cell types, at both 11- and 25-dpi.
471
472 Whereas overall cell-cell communication was increased in *Lmna* cKO hearts at the 25-
473 dpi timepoint, cardiomyocyte-to-cardiomyocyte communication strength as a whole was
474 markedly reduced in *Lmna* cKO versus *Lmna* cWT hearts at both timepoints (Figure 5B).
475 However, CellChat analysis on individual subpopulations at 11-dpi (Figure 5C, Suppl.
476 Figure S12) revealed that this reduction was primarily driven by the larger CM1 and CM2
477 subpopulations. In contrast, in *Lmna* cKO hearts, the disease-specific subpopulation CM3
478 had *increased* communication with other cardiomyocytes, as well as with myeloid
479 subpopulations Mye1 and Mye 2 and fibroblast subpopulations Fib1 and Fib4 (Figure 5C).
480 Although the CM5 subpopulation contained too few nuclei in the 11-dpi *Lmna* cWT
481 sample to assess cell-cell communication, CellChat predicted interactions between CM5
482 and the Fib1, Mye1, and Mye2 subpopulations, similar to the findings for the CM3
483 subpopulation (Suppl. Figure S12). Additionally, both Fib1 and Fib4 showed increased
484 interactions with Mye1 and Mye2 in *Lmna* cKO hearts. This finding of enhanced
485 intercellular signaling was further supported by spatial transcriptomic analysis, which
486 revealed increased spatial proximity among CM3, CM5, Fib1, Fib4, and Mye1 in *Lmna*
487 cKO compared to *Lmna* cWT hearts (Figure 5D-E, Suppl. Figure S13). Notably, Fib1 and
488 Fib4 showed a particularly pronounced shift in spatial distribution at 11-dpi, transitioning
489 from a dispersed pattern in *Lmna* cWT to a more clustered organization in the diseased
490 samples (Figure 5D).
491
492 Previous studies had reported the appearance of myofibroblast, i.e., the activated
493 fibroblast cell type primarily responsible for extracellular matrix (ECM) deposition during
494 fibrosis, in *LMNA*-DCM hearts[67]. We determined that the Fib1 fibroblast subpopulation
495 had an expression profile that most closely matched that of myofibroblasts (Figure 5F,
496 left). Additionally, the Fib1 expression profile significantly intensified in *Lmna* cKO hearts
497 over time (Figure 5F, right). Pathogenic activation of fibroblast in *Lmna* cKO hearts was
498 further supported by the CellChat prediction that cardiomyocyte and non-cardiomyocyte
499 differential interactions were largely mediated by ECM-receptor pathways (Figure 5G).
500 These results are in agreement with recent work in a similar *Lmna* cKO mouse model,
501 which found that cardiomyocytes activate fibroblasts via ECM-mediated signaling[29], and
502 suggest that fibrosis is not only a downstream consequence of cardiac dysfunction in
503 *LMNA*-DCM but directly contributes to the disease pathogenesis
504
505 The increased cell-cell communication (Figure 5C) and spatial proximity (Figure 5D-E)
506 between CM3, CM5, Fib1, Fib4, and Mye1 in *Lmna* cKO versus *Lmna* cWT hearts at 11-
507 dpi suggests a pathogenic communication network between disease-specific CM3/CM5
508 cardiomyocytes, myofibrotic fibroblasts, and infiltrating macrophages. Collectively, our
509 single-nucleus and spatial transcriptomic and immunofluorescence data indicate that
510 cardiomyocyte and non-cardiomyocyte interactions are becoming reorganized in *Lmna*
511 cKO hearts, starting in the early disease stage and progressing over time, thereby
512 promoting the inflammatory and fibrotic phenotypes observed in *LMNA*-DCM hearts.

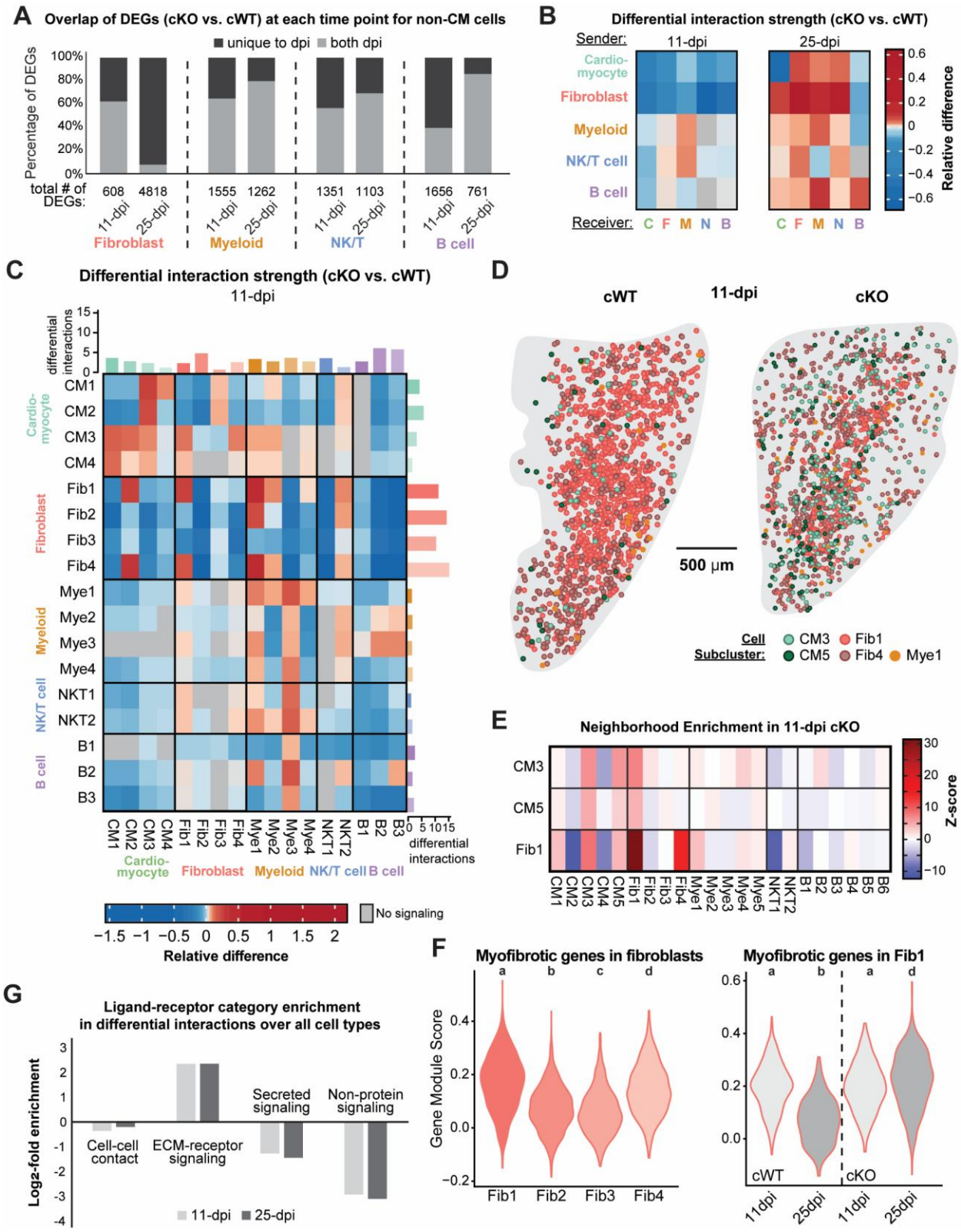

Figure 5: Prediction of intercellular signaling in *LMNA*-DCM-specific cardiomyocytes, fibroblasts, and myeloid cells reveals a fibrosis-inflammation link driven by disease-specific cardiomyocyte

population. (A) Bar chart of the percent of differentially expressed genes (DEGs) between *Lmna* cKO (cKO) and *Lmna* cWT (cWT) hearts at each time point, 11- and 25-days post infection (dpi), for individual non-cardiomyocyte (CM) cell types (separated by dotted line). DEGs unique to a time point (light gray) or represented in both (dark gray) are denoted. The total number of DEGs per condition is indicated under each column. **(B-C)** Heatmap showing relative difference (cKO versus cWT) in the interaction strength of sender (rows) and receiver (columns, initial letter) **(B)** cell types and **(C)** subpopulations at 11- (left) and 25-dpi (right). **(C)** The number of differential interactions for each row and column are indicated in the bar plot. Subpopulations with too few nuclei for cell-cell communication analysis were removed (i.e., CM5, Mye5, and B4-6). **(D)** Spatial transcriptomics annotation of cardiomyocyte (CM3, light green; CM5 dark green), fibroblast (Fib1, pink; Fib4 maroon), and myeloid (Mye1, orange) subpopulations in cWT and cKO 11-dpi ventricles (tissue boundaries shown in gray) from heart slices. **(E)** Heatmap of *z*-score neighborhood enrichment for subpopulations in 11-dpi cKO ventricles based on spatial transcriptomics. **(F)** Violin plots of gene module scores for a myofibrotic gene set in fibroblast subpopulations (left) and split by experimental condition for Fib1 (right, light gray - cWT, dark gray - cKO). Sets of points with the same letter above them are not significantly different, whereas different letters indicate $p < 0.05$, Kruskal–Wallis tests followed by pairwise Mann–Whitney U tests with Benjamini-Hochberg *p*-value adjustment. **(G)** Bar plot showing the $\log_2$-fold enrichment of particular ligand-receptor categories associated with differential interactions over all cell types by time point (light gray: 11-dpi; dark gray: 25-dpi).

Reducing NE damage in lamin A/C-deficient cardiomyocytes partially restores gene expression and substantially ameliorates *LMNA*-DCM pathology.

Our data suggest that inflammatory responses triggered by NE rupture of mechanically weaker *Lmna* cKO cardiomyocyte nuclei drive altered gene expression and pathogenesis in *LMNA*-DCM hearts. Thus, we hypothesize that reducing NE rupture should at least partially reverse transcriptional changes, even in the continued absence of lamin A/C, and ameliorate disease progression. To test this hypothesis, we generated mice with inducible, cardiomyocyte-specific expression of a dominant negative nesprin-construct, consisting of the Klarsicht, ANC-1, Syne Homology (KASH) domain of nesprin-2 (DN Kash)[68], and concurrent depletion of lamin A/C (Figure 6A). Expression of the DN Kash construct displaces endogenous nesprin proteins from the NE, resulting in LINC complex disruption and reducing cytoskeletal forces acting on the nucleus[9,10,32–35,69]. LINC complex disruption has previously been shown to reduce NE rupture and DNA damage in lamin A/C-deficient and *Lmna* mutant myoblasts[9] and isolated cardiomyocytes[10], making it particularly well-suited to test our hypothesis. Tamoxifen treatment of adult mice resulted in a significant reduction in the fraction of *Lmna* cKO cardiomyocytes with NE ruptures at the early disease stage (11-dpi; Figure 6B). Strikingly, cardiomyocyte-specific disruption of the LINC complex dramatically improved cardiac function in *Lmna* cKO animals (Figure 6C, Suppl. Figure S14A-D). Although cardiac function was not rescued completely, *Lmna* cKO mice expressing the DN Kash had near-normal lifespan, with survival extended from roughly 30 dpi to over 400-dpi, which served as our experimental endpoint. *Lmna* cWT animals with cardiac LINC complex disruption had normal survival (Figure 6D). These findings underscore the therapeutic potential of targeting the LINC complex in *LMNA*-DCM.

To investigate how LINC complex disruption affects the transcriptional landscape, especially in relation to eDEGs and their associated inflammatory and cytosolic DNA-sensing pathways, we conducted bulk RNA-seq on left ventricular tissue from *Lmna* cKO and *Lmna* cWT mice, each with and without concurrent cardiomyocyte-specific LINC

567 complex disruption. We decided to apply bulk RNA-seq to efficiently capture global
568 transcriptional changes across the left ventricle with higher sensitivity and better gene
569 coverage than offered by snRNA-seq and spatial approaches, thus providing a
570 comprehensive view of the potential rescue by DN Kash expression. Appling our bulk
571 RNA-seq analysis pipeline to *Lmna* cKO and *Lmna* cWT littermates lacking the DN Kash
572 transgene validated the progressive increase in DEGs from 11-dpi (n=208) to 25-dpi
573 (n=3426) (Suppl. Figure S15A), similarly to what we had observed in the original *Lmna*
574 cKO vs. *Lmna* cWT analysis (Figure 2B, C, Suppl. Figure S2A). Cross-referencing of gene
575 expression differences between *Lmna* cKO and *Lmna* cWT hearts lacking DN Kash
576 expression at 11- and 25-dpi identified 83 eDEGs (Suppl. Figure S15A-B). The smaller
577 number of eDEGs compared to the original study in *Lmna* cKO vs *Lmna* cWT mice without
578 the inducible DN Kash system is likely due to the subtle fold changes observed at 11-dpi.
579 At this early stage of disease, transcriptional differences are expected to be nascent and
580 potentially disease-initiating, making them particularly sensitive to biological noise,
581 mouse-to-mouse variability, and technical batch effects. Despite the smaller set of
582 eDEGs, these genes were enriched for GO terms involved in inflammation, apoptosis,
583 and innate immunity (Suppl. Figure S15C), consistent with our earlier findings in the *Lmna*
584 cKO mice (Figure 2). This suggests that even modest early transcriptional shifts may
585 reflect meaningful disease-relevant processes, although their directionality and
586 magnitude may vary depending on cohort-specific factors. In *Lmna* cWT hearts, DN Kash
587 expression cause only very minimal transcriptional changes (4 DEGs detected by 25-dpi).
588 This minimal impact on gene expression supports that any transcriptional changes
589 observed in *Lmna* cKO mice are likely disease-related rather than inherent to LINC
590 complex disruption itself.
591
592 We determined that over half of eDEGs (*n* = 44, 53%) in *Lmna* cKO hearts with LINC
593 complex disruption returned to levels statistically indistinguishable from those in *Lmna*
594 cWT controls, which we termed 'complete rescue' (Figure 6E-F, Suppl. Figure S15D). We
595 identified an additional 11 eDEGs (13%) with a 'partial rescue', i.e., their expression
596 significantly differed between *Lmna* cKO samples with and without LINC complex
597 disruption but did not entirely return to *Lmna* cWT levels (Figure 6E-F, Suppl. Figure
598 S15D). By further breaking this rescue down by time point, we determined that a small
599 fraction of eDEGs were rescued already at 11-dpi (5 eDEGs, 6%); however, the majority
600 of eDEGs (50 eDEGs, 60.2%) reached rescue levels at 25-dpi (Figure 6E). GO term
601 analysis of eDEGs showed that whereas several terms related to apoptosis and
602 inflammation were enriched in the "partial" and "complete" rescued gene set, GO terms
603 "inflammatory response" and "leukocyte chemotaxis" were still present in the "no rescue"
604 eDEGs (Figure 6G). The enrichment of GO terms associated with inflammatory pathways
605 in both the "complete" and "no rescue" eDEG categories indicates that LINC complex
606 disruption does not fully mitigate all inflammatory processes. This observation may be
607 due to residual NE damage in *Lmna* cKO mice, despite DN Kash expression (Figure 6B),
608 and the inherent multifactorial nature of inflammatory signaling. Nonetheless, the
609 improved cardiac function and survival in the *Lmna* cKO mice with LINC complex
610 disruption suggest that key pathological drivers of inflammation is mitigated. In support of
611 this idea, "Cellular response to interleukin-6" showed the strongest enrichment within GO
612 terms that were completely rescued following DN Kash expression (Figure 6G bottom).

613 IL-6 is a cytokine produced downstream of cytoplasmic DNA-sensing pathways mediated
614 by TLRs, and therefore, a potential key regulator of immune cell activation in *Lmna* cKO
615 hearts. Supporting this finding is the enrichment of “Negative regulation of cytokine
616 production” and “Endocytosis” within the partially rescued GO terms.
617 Immunofluorescence staining of IL-6 further validated the reduction of this inflammatory
618 cytokine in *Lmna* cKO hearts with DN Kash expression as compared to *Lmna* cKO hearts
619 without DN Kash expression (Figure 6H-I). Furthermore, DN Kash expression rescued
620 the aberrant expression of several key genes involved in cytosolic DNA sensing, including
621 *Rtn4*, *Ifi204*, *Tlr9*, *Il6*, *Irf7*, and *Hspa1a* (Suppl. Figure S16). Together, these results
622 suggest that the therapeutic benefits of LINC complex disruption in cardiomyocytes result
623 from reducing NE ruptures and downstream signaling, such as activation of pattern
624 recognition receptor (PRR) pathways and the production of inflammatory cytokines, like
625 IL-6.
626

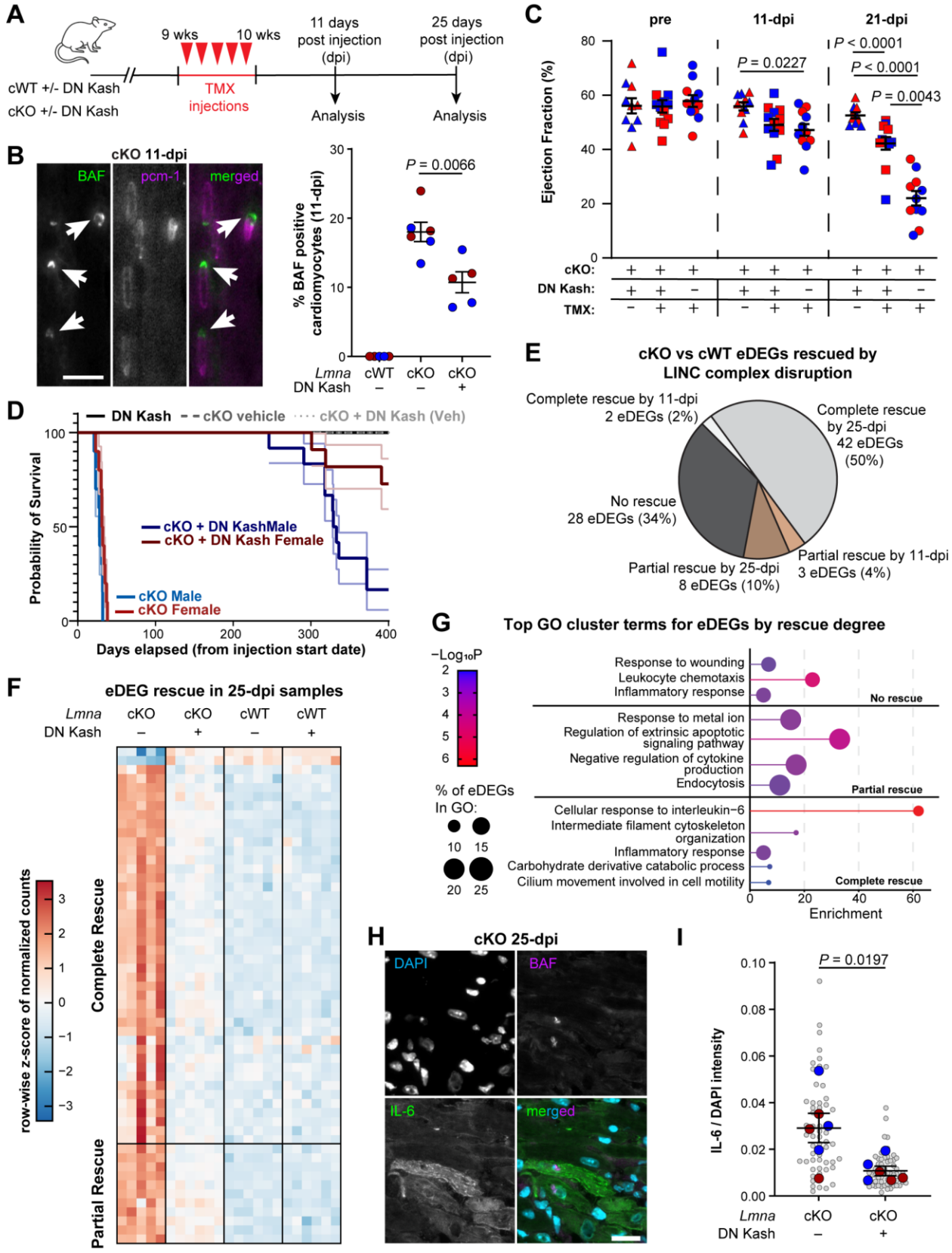
A
9 wks
10 wks
11 days post injection (dpi)
25 days post injection (dpi)
cWT +/- DN Kash
cKO +/- DN Kash
TMX injections
Analysis
Analysis
B
cKO 11-dpi
BAF
pcm-1
merged
% BAF positive cardiomyocytes (11-dpi)
P = 0.0066
Lmna
DN Kash
cWT
cKO
cKO
C
pre
11-dpi
21-dpi
Ejection Fraction (%)
P = 0.0227
P < 0.0001
P < 0.0001
P = 0.0043
cKO:
DN Kash:
TMX:
D
DN Kash
cKO vehicle
cKO + DN Kash (Veh)
Probability of Survival
cKO + DN KashMale
cKO + DN Kash Female
cKO Male
cKO Female
Days elapsed (from injection start date)
E
cKO vs cWT eDEGs rescued by LINC complex disruption
Complete rescue by 11-dpi 2 eDEGs (2%)
Complete rescue by 25-dpi 42 eDEGs (50%)
No rescue 28 eDEGs (34%)
Partial rescue by 25-dpi 8 eDEGs (10%)
Partial rescue by 11-dpi 3 eDEGs (4%)
F
eDEG rescue in 25-dpi samples
Lmna
DN Kash
cKO
cKO
cWT
cWT
row-wise z-score of normalized counts
Complete Rescue
Partial Rescue
G
Top GO cluster terms for eDEGs by rescue degree
−Log₁₀P
% of eDEGs In GO:
Response to wounding
Leukocyte chemotaxis
Inflammatory response
No rescue
Response to metal ion
Regulation of extrinsic apoptotic signaling pathway
Negative regulation of cytokine production
Endocytosis
Partial rescue
Cellular response to interleukin−6
Intermediate filament cytoskeleton organization
Inflammatory response
Carbohydrate derivative catabolic process
Cilium movement involved in cell motility
Complete rescue
Enrichment
H
cKO 25-dpi
DAPI
BAF
IL-6
merged
I
P = 0.0197
IL-6 / DAPI intensity
Lmna
DN Kash
cKO
cKO

627

Figure 6: LINC complex disruption dramatically improves cardiac function and survival in *Lmna* cKO mice by reducing NE rupture and transcriptional activation of cytosolic DNA sensing-mediated inflammation. (A) *Lmna* cKO (cKO) and *Lmna* cWT (cWT) mice with (+) and without (–) the cardiomyocyte-specific LINC complex disruption induced by expression of the dominant negative KASH protein (DN Kash) were injected with 30 mg/kg tamoxifen for 5 consecutive days, starting at 9-10 weeks of age. Following a washout period, cardiac tissues were collected for analysis at 11 dpi, i.e., an early disease stage, and at 21-25 dpi, when the cardiac phenotype is well pronounced. Functional cardiac measurements (echocardiography) were performed at the same time points. **(B)** Representative images of BAF positive (green) cardiomyocytes (pcm-1 magenta) of *Lmna* cKO mice without LINC complex disruption (left) and quantification for *Lmna* cWT and *Lmna* cKO mice with (+ DN Kash) and without LINC complex disruption (right). Arrows indicate representative cardiomyocytes. Larger colored circles represent average values for individual male (blue) or female (red) mice. *N* = 5-6 animals per genotype. **(C)** Left ventricular ejection fraction (EF), given as a percentage, measured by echocardiography either before tamoxifen (TMX) injection (pre), or at 11-dpi and 25-dpi. Symbols represent %EF of individual mice. Red symbols denote female mice, blue male mice. Error bars represent mean ± S.E.M. **(D)** Kaplan-Meier survival plot for *Lmna* cWT mice with LINC complex disruption (*Lmna* cWT + DN Kash, *10* = 5 males and 5 females), *Lmna* cKO mice treated with vehicle (*Lmna* cKO vehicle, *10* = 5 males and 5 females), *Lmna* cKO mice with DN Kash treated with vehicle (*Lmna* cKO + DN Kash, *10* = 5 males and 5 females), *Lmna* cKO mice with LINC complex disruption (*Lmna* cKO + DN Kash, *N* = 23 mice: 12 males and 11 females), and *Lmna* cKO mice (*Lmna* cKO, *N* = 20 mice: 10 males and 10 females). **(E)** Pie chart showing the fraction of emerging differentially expressed genes (eDEGs) with complete (44 eDEGs, light gray), partial (11 eDEGs, brown), or no rescue (28 eDEGs, dark gray) brought on by LINC complex disruption. **(F)** Heatmap of row-wise z-score normalized read counts for eDEGs rescued by LINC complex disruption. Rows are separated based on the degree of rescue, either complete (top) or partial (bottom). Columns, indicating individual samples, are separated by condition. **(G)** Lollipop plot of top Gene Ontology (GO) cluster terms enriched in eDEGs based on the degree of rescue, categorized as none (top), partial (middle), or complete (bottom) rescue. Color indicates the significance of enrichment, and dot size represents the percentage of eDEGs contained within the term. **H)** Representative images of *Lmna* cKO (cKO) without LINC complex disruption cardiac tissue immunofluorescently labeled for BAF (magenta), IL-6 (green) and stained for DNA with DAPI (blue). Arrows indicate representative cells. Scale bar: 20 µm. **I)** Quantification of IL-6 signal in *Lmna* cKO with (+ DN Kash) and without (– DN Kash) LINC complex disruption. Larger colored circles represent average values for individual male (blue) or female (red) mice. Smaller gray circles represent individual fields of view. *N* = 6 animals per genotype. Statistical analysis performed by two-sided *t*-test.

Discussion

We generated a novel mouse model for *LMNA*-DCM with inducible, cardiomyocyte-specific lamin A/C depletion to gain further insights into the pathogenic mechanisms responsible for the cardiac phenotypes. Using a comprehensive, temporally resolved transcriptomic analysis of cardiac tissue that combines bulk, single-nucleus, and spatially resolved RNA-seq, we identified two disease-specific cardiomyocyte subpopulations that were largely responsible for the expression of disease-driving genes, termed eDEGs (Figure 2C, Suppl. Figure S2A). These eDEGs not only corroborated previously identified pathways dysregulated in *LMNA*-DCM[20–25] but also revealed a previously unrecognized role of cytosolic pattern recognition receptor (PRR) signaling that operates independently of cGAS, which is not expressed in cardiomyocytes. Integration of single-nucleus and spatial transcriptomics further demonstrated active cell-cell communication between these disease-specific cardiomyocyte subpopulations, fibroblasts, and myeloid cells. Although previous studies had reported increased NE rupture in *Lmna*-deficient and mutant cardiomyocytes[10,29] and that LINC complex disruption improves cardiac function in *LMNA*-DCM mouse models[10,70], we here present the first evidence mechanistically

680 linking NE rupture to altered gene expression in *LMNA*-DCM. We demonstrate that LINC
681 complex disruption not only reduces NE rupture in *Lmna* cKO hearts but also rescues
682 many of the transcriptomic changes in these animals, resulting in substantially improved
683 cardiac function and overall survival. Collectively, our findings establish a mechanistic link
684 between NE rupture induced exposure of DNA to the cytosol and activation of cytosolic
685 DNA-sensing and PRR pathways, to increased intercellular signaling between
686 cardiomyocytes, fibroblasts, and innate immune cells that drive fibrosis and inflammation
687 early in *LMNA*-DCM progression.
688
689 The disease specific subpopulation of cardiomyocytes (i.e., subpopulations CM3 and
690 CM5) drive many of the transcriptional changes despite representing only a small fraction
691 of all captured cardiomyocytes (CM3: 5.72%; CM5: 5.3%). This fraction of
692 cardiomyocytes is slightly smaller in magnitude than the fraction of cardiomyocytes
693 undergoing NE rupture (Figure 6B) observed in our study and others[10,29]. This
694 underrepresentation of ruptured cardiomyocytes might be explained by the potential loss
695 of severely damaged cardiomyocytes during tissue processing for snRNA-seq, or the
696 limitations from unbiased clustering may make it difficult to efficiently segregate nuclei
697 from subpopulation CM4 from the surrounding CM3 and CM5 subpopulations. CM4,
698 despite being present in *Lmna* cWT hearts, had similar representation in *Lmna* cKO
699 hearts (Figure 2F-H) and DEG overlap with eDEGs as subpopulations CM3 and CM5 at
700 25 dpi (Figure 2GI). Moreover, several of the eDEGs identified in CM4 are driven by nuclei
701 in areas bordering CM3 and CM5 (Suppl. Figure S5D) and together, CM3, 4 and 5 make
702 up roughly 30% of the cardiomyocytes at 11 dpi, which roughly matches the fraction of
703 BAF-positive nuclei in our study (Figure 6B) and previous studies in similar *LMNA*-DCM
704 models[10,29]. Thus, it is intriguing to speculate that the disease-specific subpopulations
705 represent cardiomyocytes with damaged nuclei. However, the transient nature of NE
706 rupture and NE repair[11,71,72] and timing of cytosolic DNA sensing and PRR activation in
707 response to NE rupture makes this hypothesis challenging to confirm directly.
708
709 Reducing NE rupture in lamin A/C-deficient cardiomyocytes (Figure 6B) resulted in near-
710 complete rescue of cardiac function, survival (Figure 6C, D), and PRR gene signatures
711 (Suppl. Figure S16) in *Lmna* cKO animals. These findings support a role for NE rupture
712 as an early catalyst of disease pathology in *LMNA*-DCM. Roughly 50% of transcriptomic
713 changes in *Lmna* cKO hearts appeared downstream of NE rupture, and were rescued by
714 LINC complex disruption, suggesting that the 'gene regulation hypothesis' and the
715 'structural hypothesis'[3,73] are not mutually exclusive, and are at least in part
716 mechanistically linked. At the same time, the broad impact of NE rupture on cardiac
717 dysfunction may also explain why targeting specific pathways downstream of nuclear
718 damage, such as p53 or STING signaling, has provided only limited success in preclinical
719 *LMNA*-DCM models[22,24,26]. In contrast, disrupting the LINC complex, which reduces NE
720 rupture in cardiomyocytes results in near-complete rescue in mouse models with
721 cardiomyocyte-specific lamin A/C depletion[70,74,75] (Figure 6B-D) and significantly
722 improved survival in mice with constitutive *Lmna* mutations or deletion[10,70]. It is worth
723 noting that DN Kash acts as a competitor to endogenous KASH-domain proteins, which
724 are still actively involved in attempting to form complete LINC complexes. This may
725 explain why 10% of cardiomyocyte nuclei still undergo rupture (Figure 6B). Thus, LINC

complex disruption appears to dampen the deleterious effects of NE ruptures resulting from *Lmna* deletion, rather than fully prevent them. Nevertheless, the resulting reduction in inflammation and improvement in cardiac function are sufficient to support survival comparable to wild-type mice.

Our study further revealed significant activation of innate immunity in the *Lmna* cKO hearts, based on both immunofluorescence labeling (Figures 4B-C) and transcriptomic analyses (Figures 2D, and 4D). Activation of innate immunity has been proposed previously to be driven by the cGAS/STING pathway[24], but cardiomyocytes lack cGAS expression (Suppl. Figure S7A-D). We hypothesize that the activation of innate immunity following NE rupture is instead mediated by other components of the cytoplasmic PRR pathway[76,77], which we found to be upregulated in eDEGs (Figure 2D) and enriched in the disease-specific cardiomyocyte subpopulations CM3 and CM5 (Figures 3F-I; Figure 4E-F; Suppl. Figure S7E). At the same time, it is possible that DNA released by damaged cardiomyocytes and subsequent uptake by other cells further activate cytosolic PRR pathways in non-cardiomyocyte cell types, such as macrophages and fibroblasts. These effects, complemented by cytokine and DAMP releases downstream of cytoplasmic PRR pathways, could then additionally contribute to pathogenic processes in fibroblasts and immune cells. Indeed, reduction in CM rupture (Figure 6B) resulted in the tissue-wide reversion of activation of pathways involved in cytosolic DNA detection, inflammation, and cytokine secretion (Figure 6H and S15).

Limitations of the current study. Although the *Lmna* cKO model used in our study offers several advantages for identifying early *LMNA*-DCM disease drivers, it is important to note some limitations of our model. The genetic landscape of human *LMNA*-DCM is diverse, encompassing *LMNA* missense mutations, frame-shift mutations, and splice-site variants spanning all exons and the first 10 introns of the *LMNA* gene[78]. Since *LMNA* mutations are congenital and nearly ubiquitously expressed across cel types, they may directly affect cardiac development and the function of non-cardiomyocyte cardiac cell populations, which is not reflected in our model. We hypothesize that since non-cardiomyocyte cells in our model are not depleted for lamin A/C, and thus maintain normal cellular function[79,80], their contribution to disease progression may be disproportionally more extensive compared to constitutive mutations, leading to more severe and rapid disease onset. Furthermore, other tissues affected by *LMNA* mutations might contribute to *LMNA*-DCM disease progression and severity. Indeed, while LINC complex disruption rescue is almost complete in the *Lmna* cKO model, it is only partial in models with global *Lmna* deletion or mutation[70]. In addition, the analysis presented here focused on eDEGs, i.e., genes that show changes in expression early in disease, which become even more pronounced with disease progression. This analysis leaves out any DEGs identified at 25-dpi that were not statistically significant at the early disease timepoint (11-dpi) or that were inconsistent with the direction of change between the two timepoints. Although we assume that such genes primarily reflect the consequences of disease progression, rather than disease-driving mechanisms, they may nonetheless contribute to the disease. Lastly, the goal of this study was to identify early transcriptional changes. We recognize that transcription levels do not always correlate with protein levels, nor does the transcriptional analysis capture post-translational modifications or changes in intra- and

772 extracellular localization of proteins. Thus, although the predictions from the
773 transcriptional analysis align with our histological and functional measurements, further
774 studies are necessary to fully validate the proposed mechanisms and to explore the
775 suitability of the identified pathways as potential therapeutic targets.
776
777 In conclusion, our transcriptional analyses in *Lmna* cKO mice and littermate controls
778 reveal that early activation of cytosolic PRR and ECM changes play major roles in
779 driving *LMNA*-DCM pathology. We propose a model in which NE rupture in
780 cardiomyocytes activates cytosolic PRR pathways, independent of cGAS/STING
781 signaling, and, together with other effects triggered by loss of lamin A/C, leads to
782 substantial transcriptional and functional changes in a subset of cardiomyocytes (Figure
783 7). Signaling from these cardiomyocytes, along with fibroblast-mediated ECM
784 remodeling, potentially downstream of their own PRR activation, initiate a cascade of
785 pathogenic cell-cell communication that recruits innate immune cells and promotes
786 fibrosis. These immune cells induce inflammation via their own PRR signaling, further
787 driving disease progression. Notably, reducing NE rupture in lamin A/C-deficient
788 cardiomyocytes by LINC complex disruption rescues more than half of the detected
789 eDEGs, including a substantial reversal of PRR-driven transcriptional changes, robustly
790 improves cardiac performance, and dramatically extends survival of *Lmna* cKO mice,
791 underscoring the therapeutic potential of targeting the LINC complex or other strategies
792 to reduce NE rupture in *LMNA* DCM. Besides LINC complex disruption, which currently
793 requires genetic approaches and delivery via viral vectors that can trigger adverse
794 immune reactions, our findings suggest that interventions aimed at restoring proper cell-
795 cell-communication, and/or the aberrantly activated pathways immediately downstream
796 of fragile lamin mutant nuclei, may offer new and promising strategies for treating
797 *LMNA*-DCM.

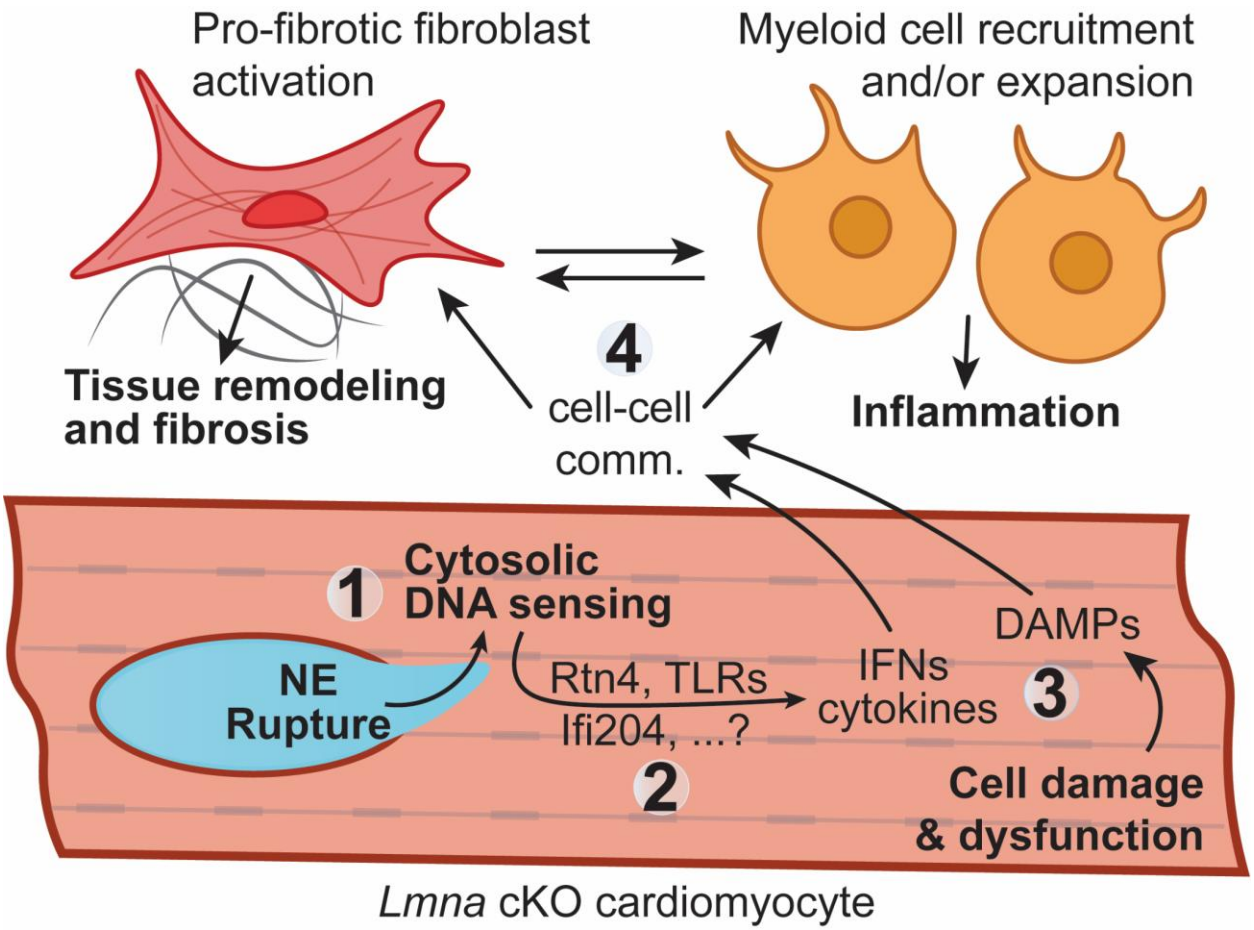

Figure 7: Cytosolic pattern recognition receptor signaling downstream of nuclear envelope rupture drives *LMNA*-DCM pathology. (1) Mechanical stress on the nuclear envelope (NE) leads to rupture in structurally compromised nuclei of *Lmna* cKO cardiomyocytes (notably subpopulations CM3 and CM5), resulting in exposure of nuclear DNA to the cytoplasm, either in the form of chromatin protrusions or cytoplasmic leakage of nuclear DNA fragments. **(2)** Cytosolic DNA is detected by cGas/STING-independent cytosolic nuclei acid sensors, such as Toll-like receptors (TLRs) regulated by Rtn4 and Ifi204, thereby activating cytoplasmic pattern recognition receptor (PRR) signaling. **(3)** PRR activation triggers the production of interferons (IFNs) and cytokines by *Lmna* cKO cardiomyocytes. Concurrently, cardiomyocytes release damage-associated molecular patterns (DAMPs) as a consequence of cellular stress and injury. **(4)** These signaling molecules mediate aberrant cell-cell communication to fibroblast (Fib1) and myeloid cells (Mye1), promoting pro-fibrotic and inflammatory signaling cascades, respectively. Crosstalk between these fibroblasts and myeloid cells further amplifies fibrosis and inflammation in the heart, ultimately impairing cardiac function. LINC complex disruption attenuates this pathological cascade by substantially reducing the frequency of NE rupture events in *Lmna* cKO cardiomyocytes.

Methods

Animals. Mice expressing a transgene containing the mouse cardiac-specific α-myosin heavy chain promoter (αMHC or Myh6) directing expression of a tamoxifen-inducible Cre recombinase (MerCreMer) in juvenile and adult cardiac myocytes (αMHC-MerCreMer) and mice possessing loxP sites flanking exon 2 of the lamin A gene (*Lmna* floxed or *Lmna*$^{fl/fl}$)[22], were obtained from The Jackson Laboratory (JAX) in a C57BL/6 background (αMHC-MerCreMer: B6.FVB(129)-A1cf$^{Tg(Myh6\text{-}cre/Esr1*)1Jmk}$/J, strain 005657; and *Lmna* floxed: *Lmna*$^{tm1.1Yxz}$/J, strain 026284, respectively) and genotyped as instructed. Mice expressing a recombinant Kash domain (DN Kash) were generated by the Hodzic lab[68]. All mice used in this study were maintained in the same C57BL/6 genetic background and backcrossed for at least three generations. To generate the inducible, cardiac specific *Lmna* deletion mouse model (*Lmna* cKO), αMHC-MerCreMer and *Lmna* floxed mice were crossed to obtain mice hemizygous for αMHC-MerCreMer and homozygous for *Lmna* floxed (*Lmna*$^{fl/fl}$). αMHC-MerCreMer hemizygous expressing wild-type *Lmna* (*Lmna*$^{+/+}$) littermates served as controls (*Lmna* cWT). To generate the inducible, cardiac specific *Lmna* deletion and LINC complex disruption mouse model (*Lmna* cKO DN Kash), αMHC-MerCreMer, DN Kash, and *Lmna* floxed mice were crossed to obtain mice hemizygous for αMHC-MerCreMer, hemizygous for DN Kash, and homozygous for *Lmna* floxed (*Lmna*$^{fl/fl}$). Littermates hemizygous for αMHC-MerCreMer and homozygous for *Lmna* floxed (*Lmna*$^{fl/fl}$), and mice hemizygous for αMHC-MerCreMer and expressing wild-type *Lmna* (*Lmna*$^{+/+}$) without DN Kash expression served as controls (*Lmna* cWT). To induce lamin A/C depletion and/or LINC complex disruption in cardiomyocytes, tamoxifen (Cayman chemicals catalog#13258) was dissolved in sunflower seed oil (Sigma catalog# 88921) to a final concentration of 30 mg/kg (3 µl/g) and injected intraperitoneally at 9-10 weeks of age for five consecutive days, followed by a one-week-long washout period. Vehicle-only injections served as additional controls. For tissue collection, mice were anesthetized at the appropriate timepoints using Isoflurane (Covetrus catalog# 11695-6777-2). Immediately following cervical dislocation, hearts were harvested, washed with ice cold 1X Phosphate Buffer Saline (PBS), and processed for downstream analysis. All experiments, including breeding, maintenance, and euthanasia of animals, were performed in accordance with relevant guidelines and ethical regulations approved by the Cornell University Institutional Animal Care and Use Committee (IACUC protocol 2011–0099). Genotyping was performed by PCR using genomic DNA isolated from tail clippings following the protocol and sequencing primers suggested by JAX. Mice were housed in a disease-free barrier facility with 12/12 h light/dark cycles.

Cardiac function. Mice were anesthetized with 2% isoflurane and placed on a stereotactic heated scanning base (37°C) attached to an electrocardiographic monitor. Left ventricular function was determined with a Vevo 2100 imaging system (VisualSonics) equipped with a MS550D transducer (22–55 MHz). Ejection fraction (EF%), fraction shortening (FS%), left ventricle diameter during systole (mm) and volume during systole (mm) were measured for at least five cardiac cycles using AM mode images. The average heart rate for all studied animals was 461 ± 24 beats per minute (BPM). Analysis was performed using the AutoLV Analysis Software (VisualSonics) and conducted by observers blinded to the mouse genotype and/or treatment groups.

859
860 **Immunofluorescence and histology of mouse tissues.** Immediately following tissue
861 collection, hearts were washed with 1X PBS and fixed in 4% paraformaldehyde (diluted
862 in 1X PBS) at 4°C overnight. Samples were stored for up to one week in 70% ethanol
863 (diluted in 1X PBS) at 4°C before being embedded in paraffin, sectioned, and stained with
864 Masson's Trichrome using standard methods at the Animal Health Diagnostic Center
865 (College of Veterinary Medicine, Cornell University). For immunofluorescence analysis,
866 samples were washed with PBS and flash frozen in Tissue-Tek® O.C.T. Compound
867 (Sakura, #4583) in an ethanol bath, followed by storage at –70°C. Frozen tissue blocks
868 were cryosectioned using an Epredia™ Microm HM525 NX Cryostat to a thickness of 5
869 µm, mounted on 25 × 75 × 1.0 mm Superfrost Plus Microscope slides (Fisherbrand® #12-
870 55015) and left to air dry for 1 hour. Samples were stored at –20°C until processed for
871 immunofluorescence staining and imaging. Prior to staining, slides containing tissue were
872 equilibrated to room temperature and rehydrated with 1X PBS for 5 minutes. When using
873 primary antibodies raised in mice, tissues were initially blocked with M.O.M® (Mouse on
874 Mouse) Blocking Reagent (Vector laboratories, Cat# MKB-2213-1, diluted 1:20 in 1X
875 PBS) for 1 hour at room temperature, followed by additional blocking and permeabilization
876 with a solution of 3% BSA, 5% filtered horse serum in PBS-T (0.05% Triton-X 100 and
877 0.03% Tween (Sigma) in 1X PBS) for 1 hour at room temperature. Tissues were then
878 incubated with primary antibodies diluted in blocking solution at 4˚C overnight. The
879 following primary antibodies were used for this study: pcm1, Santa Cruz sc398365, 1:50
880 dilution; pcm1, Sigma HPA023370, 1:500 dilution; Lamin A/C (E-1), Santa Cruz
881 sc376248, 1:100 dilution; lamin A, Sigma MAB3540, 1:100 dilution; CD68 (E3O7V), Cell
882 Signaling 97778T, 1:400 dilution; BAF, Santa Cruz sc-166324, 1:250 dilution; Rtn4,
883 Novus NB100-56681SS, 1:200 dilution. Samples were washed with PBS-T and incubated
884 for 1 hour at room temperature with AlexaFluor secondary antibodies (Invitrogen, 1:300
885 dilution) and Hoechst Nucleic Acid Stains (ThermoFisher 62249, 1:1000) in PBS-T.
886
887 **Proximity Image analysis** Images were processed using a custom CellProfiler[81] script
888 to identify regions of interest (ROIs) corresponding to DAPI-positive nuclei, Rtn4-positive
889 cells, and CD68-positive cells. DAPI-positive nuclei were identified using an Otsu two-
890 class threshold to raw DAPI-channel images, followed by smoothing and segmentation
891 based on size and shape. Rtn4-positive cells were detected using a three-class Otsu
892 threshold on raw Rtn4-channel images, smoothed, and identified based on size. CD68-
893 positive cells were identified by applying manually set threshold bounds, consistent
894 across all images, to raw CD68-channel images, followed by size-based identification.
895 The distance between CD68-positive ROIs and the nearest Rtn4-positive ROI was
896 calculated using the MeasureObjectNeighbors module. All image data was exported from
897 CellProfiler for post-processing using the ExportToSpreadsheet module.
898
899 **Western Blot analysis.** Cardiac tissue was placed in homogenization strips (VWR, Cat
900 #TN0946-08RS) in high salt RIPA buffer [12 mM sodium deoxycholate, 50 mM Tris-HCl
901 pH 8.0, 750 mM NaCl, 1% (v/v) NP-40 alternative and 0.1% (v/v) SDS in ultrapure water]
902 and a small metal ball (McMaster-Carr, Cat #1598K23). Tissues were homogenized for
903 three 3-minute cycles of 30 shakes/sec using a TissueLyser II (Qiagen). Homogenized
904 samples were sonicated (Branson 450 Digital Sonifier) for 30 s at 36% amplitude, boiled

905 for 2 min, centrifuged at 4°C for 10 min at 14,000 g and stored at −75°C. Protein
906 concentrations were determined by BCA assay, and 10 µg of total protein from each heart
907 was denatured in 5X Laemmli buffer by boiling for 3 min. Protein was loaded onto 4–12%
908 Bis-Tris gels (Invitrogen NP0322), separated for 1.5 h at 100 V, then transferred for 1 h
909 at 16 V onto PVDF membrane. Coomassie staining of the gel following transfer was used
910 to assess equal protein loading. Membranes were blocked for 1 h in blocking buffer
911 containing 3% BSA in Tris-buffered saline plus 1% Tween 20. Primary antibodies were
912 added individually overnight at 4°C diluted in blocking buffer. Primary antibodies used:
913 rabbit anti-CD68 (Cell Signaling 97778; 1:1000), rabbit anti-Rtn4 (Novus Biologicals 100-
914 56681; 1:1000), and rabbit anti-IRF7 (Invitrogen MA5-52510; 1:1000). Membranes were
915 washed 3 × 10 min, and secondary antibodies were added for 1 h at room temperature
916 in blocking buffer, followed by 3 × 10 min washed. Secondary antibodies used: Licor
917 IRDye 680RD donkey anti-mouse-IgG (LICORbio 926-68072; 1:5000) and Licor IRDye
918 800CW Donkey anti-Rabbit IgG (LICORbio 926-32213; 1:5000). Membranes were
919 imaged using Odyssey Licor scanner and then cropped and brightness and contrast was
920 adjusted using Image Studio Lite (version 5.2) software.
921
922 **Bulk RNA sequencing (RNA-seq) processing.** Left ventricle free wall tissues (excluding
923 the atria and septum) were harvested at the appropriate timepoints, flash frozen in liquid
924 nitrogen, and stored at –70°C until RNA was extracted. Frozen tissue was placed in an
925 Eppendorf tube containing one metal bead and 500 µl of TRIzol® reagent (Invitrogen,
926 #15596018). Tissues were homogenized for five 3-minute cycles of 30 shakes/sec using
927 a TissueLyser II (Qiagen) and transferred to an RNase free microfuge tube (Ambion, Cat
928 #AM12400). 1:5 chloroform was added and mixed by shaking, followed by a 5-minute
929 centrifugation at 4°C 14,000 rpm. The clear supernatant was carefully transferred to a
930 gDNA eliminator spin column (RNeasy Plus Mini Kit, Qiagen, #74136) and RNA
931 purification was performed according to manufacturer instruction. RNA quality control was
932 performed by the Cornell Genomics core facility with a fragment analyzer (Agilent) to
933 assess RNA integrity (RIN); RNA concentrations were quantified by Nanodrop
934 (ThermoFisher Scientific). To generate cDNA directional RNA-seq libraries (New England
935 Biolabs, #E7760), 1 µg of total RNA sample (with RIN ≥ 7) was enriched for mRNA (New
936 England Biolabs, #E7490) for each condition. Each sample received a unique barcode
937 for downstream multiplexing. cDNA library size distribution and concentrations were again
938 assessed by fragment analyzer and Qubit. Final libraries were pooled in equimolar
939 concentrations and sequenced. The 24 *Lmna* cKO and *Lmna* cWT samples at both time
940 points (GSE269451), used to generate data for Figure 2, were pooled 12 per lane and
941 sequenced on a NextSeq 500 (Illumina) with a 75 bp single-end kit by the Cornell
942 Genomics core facility. Libraries generated for the 48 samples (GSE304346) associated
943 with the LINC complex disruption experiment (Figure 6) were pooled into a single lane
944 and sequenced on a NovaSeq 6000 (Illumina) with an S4 flow cell and a 150 bp paired-
945 end kit by Novogene.
946
947 **Bulk RNA-seq analysis.** We used STAR software[82] (version 2.7.10a) to generate a
948 genome for read alignment using the GRCm38/mm10 (Ensembl release 102) mouse
949 FASTA and GTF files. Fastq files for the DN Kash experiment (GSE304346) had TruSeq
950 adaptors trimmed using fastp[83] (versions 0.20.0). All fastq files were aligned to the STAR

951 genome using default parameter settings, resulting in a uniquely mapped read alignment
952 ≥ 79%. Gene-level quantification was performed using the featureCounts function from
953 Subread[84] (version 2.0.1), with parameters -s 2 (for directional RNA-seq libraries), -p (for
954 paired end only with GSE304346), and the GENCODE GTF annotation file (vM23), to
955 generate a count matrix using all samples. PCA and distance correlation matrix analyses
956 were performed to identify and remove outliers (GSE269451: samples 3 and 19,
957 GSE304346: samples 16 and 43) before downstream processing. Differential gene
958 expression (DEG) analysis was performed in R (v4.1.1) by applying DESeq2[85] (v1.34.0)
959 to the input count matrix. The design formula "~genotype*timepoint", where genotypes
960 were either *Lmna* cKO, *Lmna* cWT (for GSE269451) or *Lmna* cKO, *Lmna* cWT, *Lmna*
961 cKO + DN Kash, cWT + DN Kash (for GSE304346), and timepoints were either 11- or 25-
962 days post-injection (dpi), was used. The ashr[86] shrinkage estimator was applied to all
963 DEG results. DEGs were defined as genes with $|\log_2\text{-fold change}| \geq 1$, baseMean ≥ 10,
964 and *p*-adj ≤ 0.05.
965
966 **Computation of emerging differentially expressed genes (eDEGs).** eDEGs were
967 identified based on the pipeline described below for both bulk RNA sequencing datasets
968 (GSE269451, Suppl. Figure 2A; GSE304346, Suppl. Figure 15A). We first filtered DEG
969 analysis results for *Lmna* cKO versus cWT samples at 11- and 25-dpi, based on meeting
970 a significance threshold of *p*-adj < 0.05 and a base mean expression ≥ 10. We retained
971 all 11-dpi genes that met the threshold (GSE269451: 1,405 genes, GSE304346: 2,668
972 genes) for downstream analysis, irrespective of fold-change (FC). We further refined the
973 25-dpi significance-filtered genes using a |log2 FC| ≥ 1 threshold (GSE269451: 2,951
974 DEGs, GSE304346: 3,426 DEGs), thus meeting DEG requirements outlined in the "Bulk
975 RNA-seq analysis" section. We compared the 11-dpi genes and 25-dpi DEGs, and
976 identified genes with altered expression at 11-dpi that were also found at the 25-dpi time-
977 point (GSE269451: 508 genes, GSE304346: 995 genes). ~17% of these genes
978 (GSE269451: 85 DEGs, GSE304346: 175 DEGs) had a |log2 FC| ≥ 1, thus representing
979 11-dpi DEGs. Of the genes that overlapped with 25-dpi DEGs, 496 genes (GSE269451,
980 98%) and 83 genes (GSE304346, 8%) had the same directional change at both early and
981 late timepoints (i.e., either both up- or down-regulated) and were termed emerging
982 differentially expressed genes (eDEGs). The remaining genes did not have the same
983 directional expression change at both early and late timepoints (described in Suppl. Fig.
984 S2C-D for GSE269451 and S15D-E for GSE304346).
985
986 **Classification of DEG rescue by LINC complex disruption.** To assess the extent to
987 which LINC complex disruption rescues gene misregulation in Lmna cKO hearts, we
988 analyzed DEGs identified across three pairwise comparisons:
989 (1) *Lmna* cKO hearts without LINC complex disruption versus *Lmna* cWT hearts without
990 LINC complex disruption (*Lmna* cKO vs. *Lmna* cWT) to identify genes misregulated in the
991 diseased state, (2) *Lmna* cKO hearts without LINC complex disruption versus *Lmna* cKO
992 hearts with LINC complex disruption (*Lmna* cKO vs. *Lmna* cKO + DN Kash) to evaluate
993 the impact of LINC complex disruption, and (3) *Lmna* cKO hearts with LINC complex
994 disruption versus *Lmna* cWT hearts without LINC complex disruption (*Lmna* cKO + DN
995 Kash vs. *Lmna* cWT) to determine whether gene expression returned to wild-type levels
996 with LINC complex disruption.

997 Genes were classified as rescued if they were significantly misregulated in the disease
998 (comparison 1) and significantly altered following LINC complex disruption (comparison
999 2). Complete rescue was defined as genes whose expression in *Lmna* cKO + DN-Kash
1000 hearts was no longer significantly different from *Lmna* cWT (not significant in comparison
1001 3). Partial rescue was defined as genes that remained significantly different from *Lmna*
1002 cWT despite changes following LINC complex disruption (significant in comparison 3).
1003
1004 **Single-nucleus RNA sequencing (snRNA-seq) and analysis.** Left ventricle free wall
1005 tissues (5-6 left ventricles per experimental group) were harvested from an independent
1006 subset of *Lmna* cKO and *Lmna* cWT mice at the appropriate timepoints, flash frozen in
1007 liquid nitrogen, and sent to SingulOmics (Bronx, NY, USA) for processing. There, nuclei
1008 were isolated from frozen samples and used to construct 3' single cell gene expression
1009 libraries (Next GEM v3.1) using the 10X Genomics Chromium system. Libraries were
1010 sequenced with ≈200 million PE150 reads per sample on Illumina NovaSeq 6000.
1011 Sequencing reads, including introns, were then aligned with the mouse reference genome
1012 (mm10/GENCODE vM23/Ensembl 98) using Cell Ranger[87] (v7.0.1). The Debris
1013 Identification using Expectation Maximization (DIEM) algorithm[88] was applied to remove
1014 background, keeping barcodes with debris scores < 0.5, UMI count >800, and number of
1015 features (genes) > 250. The resulting dataset was composed of 22,043 total nuclei (5,052
1016 11-dpi and 5,939 25-dpi in *Lmna* cKO; 6,300 11-dpi and 4,752 25-dpi *Lmna* cWT), before
1017 downstream filtering. snRNA-seq sample outputs from Cell Ranger were then loaded into
1018 R[89] (v4.1.1) and individually subjected to the standard Seurat[90] (v5.0.1) pipeline and
1019 sctransform. All samples were processed for ambient RNA (SoupX[91], v1.6.2) and doublet
1020 (DoubletFinder[92], v2.0.3) removal individually. Sample integration was performed with the
1021 integrated object subjected to the same standard Seurat pipeline as above, with a cluster
1022 resolution of 0.5. To annotate individual clusters with cell types using the established
1023 Azimuth reference map[93–95], mouse genes were first converted to human orthologous
1024 genes as only human heart references are available. The converted snRNA-seq dataset
1025 was then compared to the Azimuth reference map to assess prediction mapping scores[96].
1026 Cells with high-confidence annotations (prediction scores > 0.75) were used to determine
1027 cell types in each identified cluster. To identify cell type-specific subpopulations, each cell
1028 type cluster was subjected to the standard Seurat (v5.0.1) pipeline and sctransform with
1029 unique cluster resolution (0.9 for cardiomyocyte, 0.7 for myeloid cells, 0.5 for fibroblasts,
1030 0.6 for B cells, and 0.8 for NK/T cells). DEG analyses were performed for each cell type
1031 cluster using Seurat's FindMarkers function: 1) *Lmna* cKO vs. *Lmna* cWT at 11- and 25-
1032 dpi across all cells in the cluster irrespective of subpopulation, and 2) each subpopulation
1033 vs. all other subpopulations irrespective of experimental condition. Genes were required
1034 to meet a threshold of |log2 FC| ≥ 0.1, p-adj < 0.05, and for the fraction of cells expressing
1035 the gene to be ≥ 0.01 for at least one of the two queried populations. Gene modules
1036 scores were generated using Seurat's AddModuleScore function and gene lists curated
1037 by the gene ontology consortium[97,98] (GO: 0006954, 0031347, and 0008630),
1038 Harmonizome[99,100] (v3.0) (myofibroblast gene set from GeneRIF Biological Term
1039 Annotations), and peer-reviewed papers[62] (infiltrating and resident macrophage markers).
1040
1041 **Cell-cell interaction prediction.** Cell-cell communication prediction was determined
1042 using CellChat[66] (version 2.1.1). The CellChat algorithm computed the strength of specific

predicted cell-cell interactions, quantified as the sum of the communication probability of all ligand-receptor interactions, in each experimental condition[101]. CellChat objects were generated from Seurat snRNA-seq objects for each condition individually and processed using the default pipeline to identify enriched ligand-receptor interactions between all cell types and subpopulations. CellChat objects were then merged based on timepoints to perform a comparative analysis of cell-cell communication between *Lmna* cKO and *Lmna* cWT samples over time.

Functional enrichment analysis. DEGs and eDEGs Log2-fold change-ranked gene symbol lists were submitted to Metascape[47] (v3.5.20240101) and QIAGEN's Ingenuity Pathway Analysis (IPA) software[102] (v111725566) for functional enrichment analysis. All analyses used the gene ontology[97,98] (GO) biological processes database for enrichment. To perform comparative analyses between gene sets, multiple gene lists were provided simultaneously to Metascape using default parameters (i.e. p-value < 0.01, enrichment ≥ 1.5, overlap ≥ 3). Comparative analyses of predicted upstream regulators between different gene sets were performed using IPA, assuming a |z-score| > 2 and *p*-value < 0.05 as predictive of regulator activation or inhibition.

Tissue Collection and Library Preparation for Curio Seeker Spatial Transcriptomics. Isolated hearts were perfused and then coated in Tissue-Tek O.C.T. Compound (Sakura Finetek # 4583), inside cryomolds to be snap-frozen in liquid nitrogen cooled isopentane (Thermo Scientific Chemicals # AA19387AP) and stored at -80C. Frozen hearts were sectioned with a cryostat at 10 µm thick slices at -20°C. The sections were mounted on Curio Seeker tiles (Curio Biosciences) and further processed to generate spatial transcriptomics libraries.

Library Preparation and Sequencing for *Lmna* Cardiac Samples. Spatial transcriptomic libraries were prepared from heart tissue sections obtained from *Lmna* cKO and *Lmna* cWT mice at 11- and 25-days post injection (dpi). Samples were mounted directly onto barcoded Curio Seeker arrays, corresponding to tile IDs B0040_010 (*Lmna* cKO, 11-dpi), B0040_012 (*Lmna* cWT, 11-dpi), B0040_011 (*Lmna* cKO, 25-dpi), and B0040_014 (*Lmna* cWT, 25-dpi). The protocol followed Curio's spatial transcriptomics workflow, beginning with RNA hybridization and in situ reverse transcription on the array. Following enzymatic tissue digestion, spatially barcoded beads were released into solution, and second-strand cDNA synthesis and amplification were performed. Sequencing libraries were constructed using the Nextera XT DNA kit, pooled, and sequenced on an Illumina NovaSeq X Plus platform (Read 1/2: 150 bp, Index 1/2: 8 bp). Raw sequencing data were processed using the slide_snake pipeline (https://github.com/mckellardw/slide_snake). Adapter trimming and quality filtering were performed using the seeker_v3.1_internalTrim configuration (cutadapt v4.6)[103], and reads were aligned to the mouse genome (GRCm39) using STARsolo (v2.7.10b) to generate bead-resolved gene expression matrices[104].

Curio Seeker data preprocessing and quality control. For each sample, AnnData objects (v0.10.3) were generated from the raw count matrices, and spatial coordinates were assigned to beads using metadata provided by Curio Biosciences. Preprocessing

was performed using Scanpy[105,106] (v1.9.3), which included filtering out beads with fewer than 200 detected transcripts, normalizing expression values to a fixed total count per bead, and log transformation. Beads with fewer than 10 neighbors within a 100 μm radius were also excluded, as these often represent smeared or low-quality barcodes. Data were plotted, and regions of interest corresponding to the left ventricles were segmented using Napari[107]. To further reduce noise while preserving spatial structure, expression data were smoothed using the Smoothie package implementation with a Gaussian kernel of 30 μm[108].

Gene-set score calculation on spatial transcriptomics data. Gene set activity scores were then computed in Scanpy with default parameters for curated programs related to regulation of defense, interferon-beta response, intrinsic apoptosis, and inflammatory response. For each left ventricle sample, scores were compared across five cardiomyocyte states (CM1–CM5). To evaluate whether these distributions differed significantly within each heart, a Kruskal–Wallis H-test was first performed. In cases where the Kruskal–Wallis test returned a p-value < 0.05, pairwise Mann–Whitney U tests were conducted to identify specific group differences. All pairwise p-values were adjusted for multiple testing using the Benjamini–Hochberg false discovery rate (FDR) correction, applied independently within each heart sample. All tests were two-sided and implemented using the scipy.stats and statsmodels.stats Python libraries.

Cell type deconvolution. We applied cell2location[109] (v0.1.3) to deconvolve the collected spatial transcriptomics data using the single-cell dataset discussed in this work as a reference. Cell-state-specific expression signatures were estimated from the reference and projected onto the spatial data to infer the contribution of each cell state category in the spatial beads. Cell2location was run either on full heart sections or focused specifically on the left ventricle annotated regions. Model hyperparameters were set to N_cells_per_location = 1 and detection_alpha = 20.

Cardiomyocyte neighbor score calculation. Cell states were assigned to each bead based on the maximum prediction from the cell2location model. To assess the local enrichment of specific cardiomyocyte populations, we implemented a k-nearest neighbors (kNN) approach. For each bead, we computed a Cardiomyocyte neighbor score by counting how many of its 10 nearest spatial neighbors shared the same predicted cardiomyocyte state (CM1 to CM5). This analysis was performed independently for each of the segmented ventricular spatial transcriptomics objects.

Neighborhood enrichment analysis on spatial transcriptomics data. *Z*-score calculations of neighborhood enrichment was calculated using Squidpy[110] (v1.2.2) for all experimental conditions. A heatmap of this enrichment was generated with Seaborn[111] (v0.12.2). Finally, visualization of individual subpopulations across the tissue was generated through Squidpy.

Data availability. The transcriptomic datasets generated from cardiac tissue samples and used to support the conclusions in this article are limited to reviewers and journal

editors for the preprint version of the manuscript. All data will be made publicly available in the GEO repository following peer review and publication

Statistical analysis. Animals were randomly assigned to treatment groups, and experiments were conducted blinded to treatment and genotype. Since Cre expressed in the heart can be cardiotoxic at high tamoxifen doses, experiments used only low tamoxifen doses (30 mg/kg/day). Furthermore, for maximum stringency, comparisons are focused on groups in which all mice express the MCM transgene but differ in the status of the floxed *Lmna* gene. Tissues isolated from individual mice were counted as a single replicate (unless otherwise specified). Since the bulk-RNA sequencing data did not show any sex difference, male and female mice were combined for downstream transcriptomic analysis. Survival curves were generated using the Kaplan–Meier method and differences in survival tested with a Breslow test using GraphPad Prism 10. For results that follow a Gaussian distribution, the mean and standard error of the mean (SEM) were calculated; comparison between two groups used *t*-tests; ANOVA with Tukey or Dunnett post-analysis was used to test for statistical significance between more than two experimental groups. Data linearity was determined using Pearson correlation coefficients and significance calculated using the R package ggpubr[112]. The non-parametric pairwise wilcoxon rank sum test was calculated to determine significant changes in gene module scores between conditions in R.

Acknowledgments

The authors thank Stephen Weiss (University of Michigan) and Didier Hodzic (Washington University at St. Louis) for generously providing the floxed *Lmna* mice and DN Kash expressing mice, respectively. In addition, the authors thank Ern Hwei Hannah Fong for help with tamoxifen injections, and Alexander Sopilniak Mints, Hind Zahr, and Julie Heffler for help with weaning and genotyping mice. Bulk RNA sequencing was performed by the Biotechnology Resource Center (BRC) Genomics Facility (RRID:SCR_021727) at the Cornell Institute of Biotechnology.

Sources of Funding

This work was supported by awards from the National Institutes of Health (R01 HL082792, R01 AR084664, and R35 GM153257 to J.L; R01 HL160028 and R01 AI176681 to I.D.V.), the National Science Foundation (MCB-1715606 and URoL-2022048 to J.L.), the Volkswagen Foundation (A130142 to J.L.), the American Heart Association (postdoctoral fellowships 20POST35210660 to N.Z.S. and 23POST1023021 to J.M.), the Leducq Foundation (20CVD01 and 24CVD03 to J.L.), the Cornell Center for Vertebrate Genomics (CVG Scholar award to J.M.), additional ventures (990696 to I.D.V.), and generous gifts from the Mills family to J.L. The content of this manuscript is solely the responsibility of the authors and does not necessarily represent the official views of the National Institutes of Health. We acknowledge the Cornell Institute of Biotechnology's BRC Imaging Facility for use of their instruments in this study (RRID:SCR_021727).

Disclosures

No conflicts of interest to disclose.

Supplemental Material

Supplementary Figures S1-S16

1190 # References

1191

1192 1. Naetar, N., Ferraioli, S. & Foisner, R. Lamins in the nuclear interior - life outside the
1193 lamina. *J Cell Sci* **130**, 2087–2096 (2017).
1194 2. Worman, H. J. Cell signaling abnormalities in cardiomyopathy caused by lamin A/C gene
1195 mutations. *Biochem Soc Trans* **46**, 37–42 (2018).
1196 3. de Leeuw, R., Gruenbaum, Y. & Medalia, O. Nuclear Lamins: Thin Filaments with Major
1197 Functions. *Trends Cell Biol* **28**, 34–45 (2018).
1198 4. Perez-Serra, A. *et al.* A novel mutation in lamin a/c causing familial dilated cardiomyopathy
1199 associated with sudden cardiac death. *J Card Fail* **21**, 217–25 (2015).
1200 5. van Berlo, J. H. *et al.* Meta-analysis of clinical characteristics of 299 carriers of LMNA gene
1201 mutations: do lamin A/C mutations portend a high risk of sudden death? *J Mol Med Berl*
1202 **83**, 79–83 (2005).
1203 6. Arbustini, E. *et al.* Autosomal dominant dilated cardiomyopathy with atrioventricular block:
1204 a lamin A/C defect-related disease. *J Am Coll Cardiol* **39**, 981–90 (2002).
1205 7. Becane, H. M. *et al.* High incidence of sudden death with conduction system and
1206 myocardial disease due to lamins A and C gene mutation. *Pacing Clin Electrophysiol* **23**,
1207 1661–6 (2000).
1208 8. Shin, J.-Y. & Worman, H. J. Molecular Pathology of Laminopathies. *Annual Review of*
1209 *Pathology: Mechanisms of Disease* vol. 17 159–180 (2022).
1210 9. Earle, A. J. *et al.* Mutant lamins cause nuclear envelope rupture and DNA damage in
1211 skeletal muscle cells. *Nat Mater* **19**, 464–473 (2020).
1212 10. Pavlov, D. A. *et al.* Microtubule forces drive nuclear damage in LMNA cardiomyopathy.
1213 *bioRxiv* 2024.02.10.579774 (2024) doi:10.1101/2024.02.10.579774.
1214 11. Wallace, M. *et al.* Nuclear damage in LMNA mutant iPSC-derived cardiomyocytes is
1215 associated with impaired lamin localization to the nuclear envelope. *Mol Biol Cell* **34**,
1216 mbcE21100527 (2023).
1217 12. Zwerger, M. *et al.* Myopathic lamin mutations impair nuclear stability in cells and tissue and
1218 disrupt nucleo-cytoskeletal coupling. *Hum. Mol. Genet.* **22**, 2335–2349 (2013).
1219 13. Wiesel, N. *et al.* Laminopathic mutations interfere with the assembly, localization, and
1220 dynamics of nuclear lamins. *Proc. Natl. Acad. Sci.* **105**, 180–185 (2008).
1221 14. Denais, C. M. *et al.* Nuclear envelope rupture and repair during cancer cell migration.
1222 *Science* **352**, 353–358 (2016).
1223 15. Raab, M. *et al.* ESCRT III repairs nuclear envelope ruptures during cell migration to limit
1224 DNA damage and cell death. *Science* **352**, 359–362 (2016).
1225 16. Halfmann, C. T. *et al.* Repair of nuclear ruptures requires barrier-to-autointegration factor.
1226 *J. Cell Biol.* **218**, 2136–2149 (2019).
1227 17. Young, A. M., Gunn, A. L. & Hatch, E. M. BAF facilitates interphase nuclear membrane
1228 repair through recruitment of nuclear transmembrane proteins. *Mol. Biol. Cell* **31**, 1551–
1229 1560 (2020).
1230 18. Bakhoum, S. F. *et al.* Chromosomal instability drives metastasis through a cytosolic DNA
1231 response. *Nature* **553**, 467–472 (2018).
1232 19. Nader, G. P. de F., Williart, A. & Piel, M. Nuclear deformations, from signaling to
1233 perturbation and damage. *Curr. Opin. Cell Biol.* **72**, 137–145 (2021).
1234 20. Veltrop, R. J. A. *et al.* From gene to mechanics: a comprehensive insight into the
1235 mechanobiology of LMNA mutations in cardiomyopathy. *Cell Commun Signal* **22**, 197
1236 (2024).
1237 21. Zhang, X., Shao, X., Zhang, R., Zhu, R. & Feng, R. Integrated analysis reveals the
1238 alterations that LMNA interacts with euchromatin in LMNA mutation-associated dilated
1239 cardiomyopathy. *Clin Epigenetics* **13**, 3 (2021).

1240 22. Chen, S. N. *et al.* DNA Damage Response/TP53 Pathway Is Activated and Contributes to
1241 the Pathogenesis of Dilated Cardiomyopathy Associated With LMNA (Lamin A/C)
1242 Mutations. *Circ Res* **124**, 856–873 (2019).
1243 23. Cheedipudi, S. M. *et al.* Genomic Reorganization of Lamin-Associated Domains in Cardiac
1244 Myocytes Is Associated With Differential Gene Expression and DNA Methylation in Human
1245 Dilated Cardiomyopathy. *Circ Res* **124**, 1198–1213 (2019).
1246 24. Cheedipudi, S. M., Asghar, S. & Marian, A. J. Genetic Ablation of the DNA Damage
1247 Response Pathway Attenuates Lamin-Associated Dilated Cardiomyopathy in Mice. *JACC*
1248 *Basic Transl Sci* **7**, 1232–1245 (2022).
1249 25. Cho, S. *et al.* Mechanosensing by the Lamina Protects against Nuclear Rupture, DNA
1250 Damage, and Cell-Cycle Arrest. *Dev Cell* **49**, 920-935 e5 (2019).
1251 26. Kirby, T. J., Zahr, H. C., Fong, E. H. H. & Lammerding, J. Eliminating elevated p53
1252 signaling fails to rescue skeletal muscle defects or extend survival in lamin A/C-deficient
1253 mice. *Cell Death Discov* **10**, 245 (2024).
1254 27. Wu, W. *et al.* mTOR Inhibition Prolongs Survival and Has Beneficial Effects on Heart
1255 Function After Onset of Lamin A/C Gene Mutation Cardiomyopathy in Mice. *Circ Heart Fail*
1256 **17**, e011110 (2024).
1257 28. Zhang, H., Ren, L. & Wu, J. C. New Insights Into the Therapy for Lamin-Associated Dilated
1258 Cardiomyopathy. *JACC Basic Transl Sci* **7**, 1246–1248 (2022).
1259 29. En, A. *et al.* Pervasive nuclear envelope ruptures precede ECM signaling and disease
1260 onset without activating cGAS-STING in Lamin-cardiomyopathy mice. *Cell Rep.* **43**,
1261 114284 (2024).
1262 30. Pan, J. *et al.* Current understanding of the cGAS-STING signaling pathway: Structure,
1263 regulatory mechanisms, and related diseases. *Zool Res* **44**, 183–218 (2023).
1264 31. Skopelja-Gardner, S., An, J. & Elkon, K. B. Role of the cGAS–STING pathway in systemic
1265 and organ-specific diseases. *Nat. Rev. Nephrol.* **18**, 558–572 (2022).
1266 32. Lombardi, M. L. & Lammerding, J. Keeping the LINC: the importance of nucleocytoskeletal
1267 coupling in intracellular force transmission and cellular function. *Biochem. Soc. Trans.* **39**,
1268 1729–1734 (2011).
1269 33. Yerima, G., Domkam, N., Ornowski, J., Jahed, Z. & Mofrad, M. R. K. Force transmission
1270 and SUN-KASH higher-order assembly in the LINC complex models. *Biophys. J.* **122**,
1271 4582–4597 (2023).
1272 34. Lombardi, M. L. *et al.* The Interaction between Nesprins and Sun Proteins at the Nuclear
1273 Envelope Is Critical for Force Transmission between the Nucleus and Cytoskeleton*. *J.*
1274 *Biol. Chem.* **286**, 26743–26753 (2011).
1275 35. Hao, H. & Starr, D. A. SUN/KASH interactions facilitate force transmission across the
1276 nuclear envelope. *Nucleus* **10**, 73–80 (2019).
1277 36. Narula, N. *et al.* Quantitative expression of the mutated lamin A/C gene in patients with
1278 cardiolaminopathy. *J Am Coll Cardiol* **60**, 1916–20 (2012).
1279 37. Verga, L. *et al.* Loss of lamin A/C expression revealed by immuno-electron microscopy in
1280 dilated cardiomyopathy with atrioventricular block caused by LMNA gene defects.
1281 *Virchows Arch* **443**, 664–71 (2003).
1282 38. Jimenez-Alcantara, I. *et al.* LMNA p.Arg624His Variant Reduces Lamin Expression at
1283 mRNA Level: Elucidating Molecular Pathways toward Cardiac Involvement in
1284 Laminopathies. *J Cardiovasc Transl Res* (2024) doi:10.1007/s12265-024-10512-y.
1285 39. Sullivan, T. *et al.* Loss of A-type lamin expression compromises nuclear envelope integrity
1286 leading to muscular dystrophy. *J Cell Biol* **147**, 913–20 (1999).
1287 40. Mounkes, L. C., Kozlov, S. V., Rottman, J. N. & Stewart, C. L. Expression of an LMNA-
1288 N195K variant of A-type lamins results in cardiac conduction defects and death in mice.
1289 *Hum Mol Genet* **14**, 2167–80 (2005).

1290 41. Arimura, T. *et al.* Mouse model carrying H222P-Lmna mutation develops muscular
1291 dystrophy and dilated cardiomyopathy similar to human striated muscle laminopathies.
1292 *Hum Mol Genet* **14**, 155–69 (2005).
1293 42. Sztretye, M. *et al.* From Mice to Humans: An Overview of the Potentials and Limitations of
1294 Current Transgenic Mouse Models of Major Muscular Dystrophies and Congenital
1295 Myopathies. *Int J Mol Sci* **21**, (2020).
1296 43. Stewart, C. L., Kozlov, S., Fong, L. G. & Young, S. G. Mouse models of the laminopathies.
1297 *Exp Cell Res* **313**, 2144–56 (2007).
1298 44. van Rijsingen, I. A. W. *et al.* Gender-specific differences in major cardiac events and
1299 mortality in lamin A/C mutation carriers. *Eur. J. Heart Fail.* **15**, 376–384 (2013).
1300 45. Zhang, H., Kieckhaefer, J. E. & Cao, K. Mouse models of laminopathies. *Aging Cell* **12**, 2–
1301 10 (2013).
1302 46. Ashburner, M. *et al.* Gene ontology: tool for the unification of biology. The Gene Ontology
1303 Consortium. *Nat Genet* **25**, 25–9 (2000).
1304 47. Zhou, Y. *et al.* Metascape provides a biologist-oriented resource for the analysis of
1305 systems-level datasets. *Nat. Commun.* **10**, 1523 (2019).
1306 48. Muchir, A. *et al.* Activation of MAPK pathways links LMNA mutations to cardiomyopathy in
1307 Emery-Dreifuss muscular dystrophy. *J Clin Invest* **117**, 1282–93 (2007).
1308 49. Anderson, C. L. *et al.* Global Proteomic Analysis Reveals Alterations in Differentially
1309 Expressed Proteins between Cardiopathic Lamin A/C Mutations. *J Proteome Res* **23**,
1310 1970–1982 (2024).
1311 50. Reichart, D. *et al.* Pathogenic variants damage cell composition and single cell
1312 transcription in cardiomyopathies. *Science* **377**, eabo1984 (2022).
1313 51. Rodriques, S. G. *et al.* Slide-seq: A scalable technology for measuring genome-wide
1314 expression at high spatial resolution. *Science* **363**, 1463–1467 (2019).
1315 52. Gupta, P. *et al.* Genetic and ultrastructural studies in dilated cardiomyopathy patients: a
1316 large deletion in the lamin A/C gene is associated with cardiomyocyte nuclear envelope
1317 disruption. *Basic Res Cardiol* **105**, 365–77 (2010).
1318 53. Nikolova, V. *et al.* Defects in nuclear structure and function promote dilated
1319 cardiomyopathy in lamin A/C-deficient mice. *J Clin Invest* **113**, 357–69 (2004).
1320 54. Zhong, S. *et al.* Relationship between the cGAS−STING and NF-κB pathways-role in
1321 neurotoxicity. *Biomed. Pharmacother.* **175**, 116698 (2024).
1322 55. Baldarelli, R. M. *et al.* Mouse Genome Informatics: an integrated knowledgebase system
1323 for the laboratory mouse. *Genetics* **227**, (2024).
1324 56. Kimura, T. *et al.* Endoplasmic Protein Nogo-B (RTN4-B) Interacts with GRAMD4 and
1325 Regulates TLR9-Mediated Innate Immune Responses. *J. Immunol.* **194**, 5426–5436
1326 (2015).
1327 57. Chang, X. *et al.* The role of IFI16 in regulating PANoptosis and implication in heart
1328 diseases. *Cell Death Discov.* **10**, 204 (2024).
1329 58. Chen, Z., Behrendt, R., Wild, L., Schlee, M. & Bode, C. Cytosolic nucleic acid sensing as
1330 driver of critical illness: mechanisms and advances in therapy. *Signal Transduct. Target.*
1331 *Ther.* **10**, 90 (2025).
1332 59. Abe, T., Marutani, Y. & Shoji, I. Cytosolic DNA-sensing immune response and viral
1333 infection. *Microbiol. Immunol.* **63**, 51–64 (2019).
1334 60. Wang, E. *et al.* The Molecular Role of Immune Cells in Dilated Cardiomyopathy. *Med.*
1335 *Kaunas* **59**, (2023).
1336 61. Gerbino, A. *et al.* Pro-inflammatory cytokines as emerging molecular determinants in
1337 cardiolaminopathies. *J Cell Mol Med* **25**, 10902–10915 (2021).
1338 62. Revelo, X. S. *et al.* Cardiac Resident Macrophages Prevent Fibrosis and Stimulate
1339 Angiogenesis. *Circ. Res.* **129**, 1086–1101 (2021).

1340 63. Ma, M., Jiang, W. & Zhou, R. DAMPs and DAMP-sensing receptors in inflammation and
1341 diseases. *Immunity* **57**, 752–771 (2024).
1342 64. Turner, N. A. Inflammatory and fibrotic responses of cardiac fibroblasts to myocardial
1343 damage associated molecular patterns (DAMPs). *J. Mol. Cell. Cardiol.* **94**, 189–200
1344 (2016).
1345 65. Kendall, R. T. & Feghali-Bostwick, C. A. Fibroblasts in fibrosis: novel roles and mediators.
1346 *Front. Pharmacol.* **5**, 123 (2014).
1347 66. Jin, S., Plikus, M. V. & Nie, Q. CellChat for systematic analysis of cell-cell communication
1348 from single-cell and spatially resolved transcriptomics. *bioRxiv* 2023.11.05.565674 (2023)
1349 doi:10.1101/2023.11.05.565674.
1350 67. Jin, B., Zhu, J., Shi, H.-M., Wen, Z.-C. & Wu, B.-W. YAP activation promotes the
1351 transdifferentiation of cardiac fibroblasts to myofibroblasts in matrix remodeling of dilated
1352 cardiomyopathy. *Braz. J. Med. Biol. Res.* **52**, (2019).
1353 68. Razafsky, D. & Hodzic, D. Temporal and tissue-specific disruption of LINC complexes in
1354 vivo. *genesis* **52**, 359–365 (2014).
1355 69. Crisp, M. *et al.* Coupling of the nucleus and cytoplasm: role of the LINC complex. *J. Cell*
1356 *Biol.* **172**, 41–53 (2006).
1357 70. Chai, R. J. *et al.* Disrupting the LINC complex by AAV mediated gene transduction
1358 prevents progression of Lamin induced cardiomyopathy. *Nat Commun* **12**, 4722 (2021).
1359 71. Kalukula, Y., Stephens, A. D., Lammerding, J. & Gabriele, S. Mechanics and functional
1360 consequences of nuclear deformations. *Nat Rev Mol Cell Biol* **23**, 583–602 (2022).
1361 72. Mannino, P. J. & Lusk, C. P. Quality control mechanisms that protect nuclear envelope
1362 identity and function. *J Cell Biol* **221**, (2022).
1363 73. Shin, J.-Y. & Worman, H. J. Molecular Pathology of Laminopathies. *Annu. Rev. Pathol.*
1364 *Mech. Dis.* **17**, 159–180 (2022).
1365 74. Tan, C. Y. *et al.* Systematic in vivo candidate evaluation uncovers therapeutic targets for
1366 LMNA dilated cardiomyopathy and risk of Lamin A toxicity. *J. Transl. Med.* **21**, 690 (2023).
1367 75. Leong, E. L. *et al.* Nesprin-1 LINC complexes recruit microtubule cytoskeleton proteins and
1368 drive pathology in Lmna-mutant striated muscle. *Hum Mol Genet* **32**, 177–191 (2023).
1369 76. Thompson, M. R., Kaminski, J. J., Kurt-Jones, E. A. & Fitzgerald, K. A. Pattern recognition
1370 receptors and the innate immune response to viral infection. *Viruses* **3**, 920–40 (2011).
1371 77. Li, D. & Wu, M. Pattern recognition receptors in health and diseases. *Signal Transduct*
1372 *Target Ther* **6**, 291 (2021).
1373 78. Bonne, G. The UMD-LMNA mutations database. http://www.umd.be/LMNA/ (2020).
1374 79. Wang, Y. *et al.* The Dual Roles of Lamin A/C in Macrophage Mechanotransduction. *Cell*
1375 *Prolif.* **58**, e13794 (2024).
1376 80. Rouhi, L. *et al.* Deletion of the Lmna gene in fibroblasts causes senescence-associated
1377 dilated cardiomyopathy by activating the double-stranded DNA damage response and
1378 induction of senescence-associated secretory phenotype. *J. Cardiovasc. Aging* **2**, 30
1379 (2022).
1380 81. Stirling, D. R. *et al.* CellProfiler 4: improvements in speed, utility and usability. *BMC*
1381 *Bioinformatics* **22**, 433 (2021).
1382 82. Dobin, A. *et al.* STAR: ultrafast universal RNA-seq aligner. *Bioinformatics* **29**, 15–21
1383 (2013).
1384 83. Chen, S., Zhou, Y., Chen, Y. & Gu, J. fastp: an ultra-fast all-in-one FASTQ preprocessor.
1385 *Bioinformatics* **34**, i884–i890 (2018).
1386 84. Liao, Y., Smyth, G. K. & Shi, W. featureCounts: an efficient general purpose program for
1387 assigning sequence reads to genomic features. *Bioinformatics* **30**, 923–30 (2014).
1388 85. Love, M. I., Huber, W. & Anders, S. Moderated estimation of fold change and dispersion
1389 for RNA-seq data with DESeq2. *Genome Biol* **15**, 550 (2014).
1390 86. Stephens, M. *et al.* ashr: Methods for Adaptive Shrinkage, using Emperical Bayes. (2023).

87. Zheng, G. X. *et al.* Massively parallel digital transcriptional profiling of single cells. *Nat Commun* **8**, 14049 (2017).
88. Alvarez, M. *et al.* Enhancing droplet-based single-nucleus RNA-seq resolution using the semi-supervised machine learning classifier DIEM. *Sci Rep* **10**, 11019 (2020).
89. R Core Team. R: A language and environment for statistical computing. R Foundation for Statistical Computing. (2021).
90. Hao, Y. *et al.* Dictionary learning for integrative, multimodal and scalable single-cell analysis. *Nat. Biotechnol.* **42**, 293–304 (2024).
91. Young, M. D. & Behjati, S. SoupX removes ambient RNA contamination from droplet-based single-cell RNA sequencing data. *Gigascience* **9**, (2020).
92. McGinnis, C. S., Murrow, L. M. & Gartner, Z. J. DoubletFinder: Doublet Detection in Single-Cell RNA Sequencing Data Using Artificial Nearest Neighbors. *Cell Syst* **8**, 329-337 e4 (2019).
93. Hocker, J. D. *et al.* Cardiac cell type-specific gene regulatory programs and disease risk association. *Sci Adv* **7**, (2021).
94. Koenig, A. L. *et al.* Single-cell transcriptomics reveals cell-type-specific diversification in human heart failure. *Nat Cardiovasc Res* **1**, 263–280 (2022).
95. Litvinukova, M. *et al.* Cells of the adult human heart. *Nature* **588**, 466–472 (2020).
96. Hao, Y. *et al.* Integrated analysis of multimodal single-cell data. *Cell* **184**, 3573-3587 e29 (2021).
97. Ashburner, M. *et al.* Gene Ontology: tool for the unification of biology. *Nat. Genet.* **25**, 25–29 (2000).
98. The Gene Ontology Consortium *et al.* The Gene Ontology knowledgebase in 2023. *Genetics* **224**, iyad031 (2023).
99. Rouillard, A. D. *et al.* The harmonizome: a collection of processed datasets gathered to serve and mine knowledge about genes and proteins. *Database* **2016**, baw100 (2016).
100. Diamant, I., Clarke, D. J. B., Evangelista, J. E., Lingam, N. & Ma'ayan, A. Harmonizome 3.0: integrated knowledge about genes and proteins from diverse multi-omics resources. *Nucleic Acids Res.* **53**, D1016–D1028 (2025).
101. Jin, S. *et al.* Inference and analysis of cell-cell communication using CellChat. *Nat Commun* **12**, 1088 (2021).
102. Kramer, A., Green, J., Pollard, J. & Tugendreich, S. Causal analysis approaches in Ingenuity Pathway Analysis. *Bioinformatics* **30**, 523–30 (2014).
103. Martin, M. Cutadapt removes adapter sequences from high-throughput sequencing reads. *EMBnet.journal* **17**, 10–12 (2011).
104. Kaminow, B., Yunusov, D. & Dobin, A. STARsolo: accurate, fast and versatile mapping/quantification of single-cell and single-nucleus RNA-seq data. 2021.05.05.442755 Preprint at https://doi.org/10.1101/2021.05.05.442755 (2021).
105. Wolf, F. A., Angerer, P. & Theis, F. J. SCANPY: large-scale single-cell gene expression data analysis. *Genome Biol.* **19**, 15 (2018).
106. Virshup, I., Rybakov, S., Theis, F. J., Angerer, P. & Wolf, F. A. anndata: Access and store annotated data matrices. *J. Open Source Softw.* **9**, 4371 (2024).
107. Sofroniew, N. *et al.* napari: a multi-dimensional image viewer for Python. Zenodo https://doi.org/10.5281/zenodo.15779115 (2025).
108. Holdener, C. & De Vlaminck, I. Smoothie: Efficient Inference of Spatial Co-expression Networks from Denoised Spatial Transcriptomics Data. *BioRxiv Prepr. Serv. Biol.* 2025.02.26.640406 (2025) doi:10.1101/2025.02.26.640406.
109. Kleshchevnikov, V. *et al.* Cell2location maps fine-grained cell types in spatial transcriptomics. *Nat. Biotechnol.* **40**, 661–671 (2022).
110. Palla, G. *et al.* Squidpy: a scalable framework for spatial omics analysis. *Nat. Methods* **19**, 171–178 (2022).

111. Waskom, M. L. seaborn: statistical data visualization. *J. Open Source Softw.* **6**, 3021 (2021).
112. Kassambara, A. ggpubr: ‘ggplot2’ Based Publication Ready Plots. R package version 0.6.0. (2023).